THERMOCHEMICAL MODELLING AND DIRECTED ENERGY DEPOSITION OF COPPER-NICKEL FUNCTIONALLY GRADIENT MATERIALS

by

MUHAMMED ENES BALKAN

Submitted to the Graduate School of Engineering and Natural Sciences

in partial fulfillment of the requirements for the degree of

Master of Science

SABANCI UNIVERSITY

December 2021

THERMOCHEMICAL MODELLING AND DIRECTED ENERGY DEPOSITION OF COPPER-NICKEL FUNCTIONALLY GRADIENT MATERIALS

Approved by:

Prof. Dr. Bahattin Koç ……..

(Thesis Supervisor)

Prof. Dr. Cevat Bora Derin …….

Asst. Prof. Dr. Eda Aydoğan ……..

Date of Approval: Dec 15, 2021

ABSTRACT

THERMOCHEMICAL MODELLING AND DIRECTED ENERGY DEPOSITION OF COPPER-NICKEL FUNCTIONALLY GRADIENT MATERIALS

MUHAMMED ENES BALKAN

Manufacturing Engineering MSc. Dissertation, December 2021

Thesis Supervisor: Prof. Dr. Bahattin KOÇ

Keywords: Additive Manufacturing, Thermochemical Computational Modelling, Directed Energy Deposition, Microstructure

In recent years, advances in metal alloys and composite materials have improved the properties of constituent Materials and their homogenous properties throughout the structures. However, in certain critical applications in aerospace, military and nuclear industries, different functionalities and material properties are needed at different locations of the part. Multi-material structurers can provide massive heat conduction, wear resistance, corrosion and oxidation resistance properties provide by these several materials together. However, manufacturing such structures is still challenging. Although, traditional manufacturing methods are already used to produce multi-material structures, components often fail because of the dissimilarity between the different materials and not being able to control the material gradient and composition. Recently, additive manufacturing (AM) was recognized as a promising technique to control the manufacturing process and fabricate functionally graded materials (FGM). Because of that, In this research, development of a CuSn10-In718 functionally gradient material by

using directed energy deposition (DED) additive manufacturing process is investigated. The relation between process parameters and their corresponding material properties are analyzed for obtaining optimum process parameters. Furthermore, a thermochemical computational modeling was used to determine the viability of the FGM structure fabricated by DED technique. Microstructural and elemental composition investigation has been done by using scanning electron microscopy (SEM), back scattered electron detector (BSE), x-ray diffractometer (XRD) and energy dispersive spectroscopy (EDS).

ÖZET

YÖNLENDİRİLMİŞ ENERJİ BİRİKİMİ İLE BAKIR-NİKEL FONKSİYONEL GRADYAN MALZEME ÜRETİMİ VE TERMOKİMYASAL MODELLEMESİ

MUHAMMED ENES BALKAN

Üretim Mühendisliği, Yüksek Lisans Savunması, Aralık 2021

Tez Danışmanı: Prof. Dr. Bahattin KOÇ

Anahtar Kelimeler: Eklemeli İmalat, Termokimyasal Sayısal Modelleme, Yönlendirilmiş Enerji Birikimi, Mikroyapı

Son yıllarda metal alaşımları ve kompozit malzemelerdeki ilerlemeler, yapıdaki bileşenlerin ve homojen özelliklerini iyileştirmiştir, ancak havacılık, savunma ve nükleer endüstrilerdeki bazı kritik uygulamalarda, farklı konumlarda farklı işlevselliklere ve malzeme özelliklerine ihtiyaç duyulmaktadır. Bunun başlıca nedeni iki malzemenin bir araya geldiğinde sahip olduğu yüksek ısı iletimi, aşınma dayanımı, korozyon ve oksidasyon dayanımı özellikleridir. Ancak bu tür yapıların üretilmesi bazı zorluklar içermektedir. Günümüzde geleneksel imalat yöntemleriyle çoklu malzeme yapıları üretimi mümkün olsa da, yapı içinde bulunan farklı malzemelerin birbirine göre farklılıkları ve geleneksel imalat yöntemlerinin getirdiği proses kontrol kısıtlamaları nedenleriyle bir çok başarısız son ürün elde edilmektedir. Son zamanlarda, eklemeli imalat (AM) üretim proses parametrelerinin kontrolü ve ileri teknoloji sistemler için fonksiyonel gradyan malzeme üretimi (FGM) kapabilitesiyle umut vadeden bir imalat yöntemi olarak görülmektedir. Bu nedenlerden yola çıkarak, bu çalışma kapsamında,

yönlendirilmiş enerji birikimi (DED) eklemeli imalat yöntemi kullanılarak CuSn10-In718 fonksiyonel gradyan malzeme üretim prosesinin geliştirilmesi ve proses parametreleriyle mikroyapı özellikleri arasındaki ilişkinin araştırılması hedeflenmiştir. Ayrıca, DED tekniği ile üretilen FGM yapısının üretim koşullarını belirlemek için termokimyasal bir hesaplama modellemesi kullanılmıştır. Mikroyapı ve element kompozisyonu incelemeleri, taramalı elektron mikroskobu (SEM), geri saçılmış elektron kırınımı (BSE), x-ışınları kırınımölçeri (XRD) ve enerji dağılımlı izgeölçümü (EDS) kullanılarak yapılmıştır.

ACKNOWLEDGEMENTS

First, I would like to express my sincere gratitude to my advisor Prof. Dr. Bahattin Koç. His immense knowledge, guidance and support throughout the thesis process gave me courage and kept me going forward. I would also like to express my gratitudes to Assistant Professor Eda Aydoğan, Prof. Dr. Cevat Bora Derin and Dr. Murat Işık for their unlimited support and guidance throughout the research process.

I would like to thank Fatih Polat and Ferdows Afghah for their technical contributions and supports during the laboratory sessions. I would also like to acknowledge the opportunities given by the Sabancı University Integrated Manufacturing Research and Application Center and technical staff. By using the cutting-edge technological instruments in this center, my research capabilities have been leveled up.

In addition, I would like to express my special thanks to my family for their endless love. They bear with me through my hardest stages in the thesis process. I can never express enough how grateful I am to have them.

TABLE OF CONTENTS

ABSTRACT iv

ÖZET vi

ACKNOWLEDGEMENTS viii

LIST OF FIGURES xi

LIST OF TABLES xiii

LIST OF SYMBOLS AND ABBREVIATIONS xiv

1. INTRODUCTION 1

2. LITERATURE REVIEW 4

2.1. Additive Manufacturing 4

2.2. Functionally Graded Materials 5

2.3. Additive Manufacturing Methods For Functionally Graded Materials 5

2.3.1 Laser-based additive manufacturing methods 6

2.4. Challenges and Possible Solutions Related FGM Manufacturing With Metal AM Technology 8

2.4.1. Incongruity Between Alloys 9

2.4.2. Process Modelling 11

2.4.3. Thermochemical Modelling Approach 12

3. EXPERIMENTAL STUDY AND THERMOCHEMICAL MODELLING 14

3.1. Computer Aided Manufacturing (CAM) 16

3.2. Process Parameters Development 18

3.2.1. Optimizing CuSn10 and In718 Process Parameters 19

3.2.2 Optimizing CuSn10-In718 FGM Process Parameters 24

3.3. Characterization of Inconel 718-CuSn10 Gradient Structure 27

3.4. Thermodynamic Computation 29

3.4.1. CALPHAD Approach 30

3.4.2. Scheil Solidification Model 31

4. RESULTS AND DISCUSSION 32

5. CONCLUSION 48

References 50

LIST OF FIGURES

Figure 1 Additive Manufacturing Process Steps 4
Figure 2 (a) LPBF process demonstration [45] (b) DED process demonstration [46]. ... 8
Figure 3 Schematic of gradient structure manufacturing by DED process [57]. b-g) Demonstration of various deposition examples for FGM structures [58] 8
Figure 4 Failure examples of dissimilar bimetalic gradient structures; (a) Ti-6Al-4 V to Invar [61], and (b) Ti-6Al-4 V to V to 304 L [58]..... 10
Figure 5 Failure images of GRCop-84 - Inconel 718 FGM deposition: (a) As built sample, (b) bonding and diffusion problems GRCop-84 on Inconel 718, and (c) GRCop-84 - Inconel 718 bonding problems [66]. 11
Figure 6 Simulation of toolpath strategies of (a,c,e) zigzag, (b,d,f) spiral [69]..... 12
Figure 7 DMG Mori Seiki LASERTEC 65 DED Hybrid [75] 15
Figure 8 Digital copy of LASERTEC 65 DED system 16
Figure 9 Identification of additive structure and foundation face 17
Figure 10 Process parameter identification 17
Figure 11 Deposition assessment through CAM program..... 18
Figure 12 Failed CuSn10 trials due to overheat and overdeposition 20
Figure 13 Eclipse LV100ND (NIKON) [81] 21
Figure 14 Micrograph images of CuSn10 fabricated with 196.36 $j/mm3$ cross section results 21
Figure 15 Micrograph image of CuSn10 fabricated with 122,18 $j/mm3$ cross section results 22
Figure 16 Micrograph image of CuSn10 fabricated with 146.62 $j/mm3$ cross section results 22
Figure 17 Optimized CuSn10 Structure..... 23
Figure 18 Optimized In718 Structure 24
Figure 19 FGM Single track trials 25
Figure 20 Optimized single track trial (No:5) 26

Figure 21 Inconel 718 – CuSn10 gradient structure: (a) optimized 30x30x30 mm cubic, (b) cross section view of cubic in build direction 27
Figure 22 Struers Discotom 10 [82] 28
Figure 23 Leo SUPRA 35VP FEG-SEM measurement device [83] 29
Figure 24 Schematic of CALPHAD Approach [88] 30
Figure 25 (a) Paths of possible gradients in a ternary phase. (b) Al–Ti–V (c) Fe–Ni–Cr phase diagrams demonstrating absence of brittle phases in gradient paths (58) 31
Figure 26 SEM images of gradient structure from three different regions with 5 mm interval along build direction 32
Figure 27 EDS mapping results: (a) SEM image of the investigated area, (b) achieved and desired elemental compositions in weight percent, (c-h) EDS mapping for Ni, Cu, Cr, Fe, Sn, Nb 34
Figure 28 Non-equilibrum cooling calculation of 50:50 mixture (by weight) of CuSn10:Inconel718 alloy using FactSage™. 36
Figure 29 Back scattered electron detector image of Inconel 718 – CuSn10 gradient structures with the paths adjusted for elemental analysis by energy dispersive spectroscopy 37
Figure 30 The EDS analysis results of the locations shown in Fig 29. And possible phases 38
Figure 31 Back scattered electron detector image of Inconel 718 – CuSn10 gradient structures with the paths adjusted for elemental analysis by energy dispersive spectroscopy Nb Rich Location 39
Figure 32 The EDS analysis results of the location 5 shown in Fig 31. And possible phases 40
Figure 33 X-Ray diffraction results of In718-CuSn10 FGM structure 41
Figure 34 INNOVATEST Falcon 500 Microhardness Tester [102] 41
Figure 35 Microhardness profiles of 50%-50% In718-CuSn10 FGM (blue line), In718 (grey line), CuSn10 (orange line) structures 42
Figure 36 NETZSCH LFA 457 MicroFlash®[104] 43
Figure 37 Thermal diffusivity measurements for In718, CuSn10 and FGM structures . 44
Figure 38 NETZSCH STA 449 F3 Jupiter® [106] 45
Figure 39 Specific heat capacity measurements for In718, CuSn10 and FGM structures 46
Figure 40 Thermal conductivity values for In718, CuSn10 and FGM structures 47

LIST OF TABLES

Table 1: Metal powder chemical compositions in weight percent 15
Table 2: 15 mm -15 mm – 20 mm CuSn10 cubic trials..... 20
Table 3: Optimized DED process parameters of CuSn10 23
Table 4: Optimized DED process parameters of In718..... 24
Table 5: Single track trial process parameters..... 25
Table 6: Optimized process parameters for gradient single track 26
Table 7: Optimized process parameters of gradient cubic structure..... 27

LIST OF SYMBOLS AND ABBREVIATIONS

AM	Additive Manufacturing
DED	Directed Energy Deposition
SLM	Selective Laser Melting
FGM	Functionally Graded Materials
SEM	Scanning Electron Microscopy
XRD	X-Ray Diffractometer
BSE	Back Scattered Electron Detector
EDS	Energy Dispersive Spectroscopy
FSW	Friction Stir Welding
CALPHAD	Calculation of Phase Diagrams
CAD	Computer Aided Design
PM	Powder Metallurgy
LPBF	Laser Powder Bed Fusion
EBM	Electron Beam Melting
LENS	Laser Engineered Net Shaping
LMD	Laser Metal Deposition
EBFFF	Electron Beam Free Form Fabrication
WAAM	Wire Arc Additive Manufacturing
FG	Functionally Graded

CAM	Computer Aided Manufacturing
CNC	Computer Numerical Control
ASTM	American Society for Testing and Materials
HV	Vickers Hardness
E	Total Energy Input Per Volume
P	Laser Power
v	Scan Speed
h	Layer Thickness
t	Hatch Distance
C_s	Solid Composition
C_l	Liquid Composition
C_0	Initial Point
k	Local Equilibrium Partition Coefficient
f_s	Fraction of The Solid Phase
G	Temperature Gradient
V	Solidification Velocity
α	Thermal Diffusivity
λ	Thermal Conductivity
ρ	Density
c_p	Specific Heat Capacity

1. INTRODUCTION

Metal alloys or composite materials have improved the properties of constituent materials, their properties are mostly homogenous throughout the structures. However, in certain critical applications, different functionalities and material properties are needed at different locations of the part [1]. Metal-Ceramic composites for thermal barrier structures, heat protection sheets, low temperature resistant nickel-titanium thermal barriers are some examples of multi material structures used in aerospace, jet engine control systems and space shuttle projects [2]. Moreover, parts possessing long thermal fatigue, thermal crack and erosion resistance are needed for nuclear applications. To overcome these challenging requirements, multi material structures could be used. In general, the parts utilized in aerospace and nuclear industries experience severe thermal gradients, and such phenomena demand different structural behavior in different locations of the structure. For a single part, a simultaneous demand for oxidation, corrosion, and wear resistances, and high thermal conductivity shall sometimes be needed in different regions of the structure [3-6] and thus bringing the need of combining different materials in a single structure [3-7].

To combine different materials, traditional fusion welding methods are still of use. This process needs a transaction layer between two different materials to avoid the occurrence of cracking [8]. Friction stir welding (FSW) is a fusion welding method and is used to manufacture multi material structures. Nonetheless, using FSW and traditional fusion welding processes, the formation of the cracks, large heat affected zone and other microstructural defects are inherently triggered due to massive heat input. FSW process also leads into thermal residual stresses in the final structure due to local small transition

zone between two unsimilar materials; however, one can overcome this problem by introducing a larger gradient zone between two materials [9-15]. Since the directly bonded multi material structures suffer from cracking and delamination issues originated from dissimilar material properties of the combining metals, functionally graded materials (FGM) have been proposed. By using such materials, creating gradual changes in material properties are realized, and above-mentioned problems could be eliminated [16], although, research on the FGM method is still ongoing.

The need of advanced structures for the gas turbine engine and rocket engine parts are steadily becoming worldwide as mission profiles for such technologies get harder. To this end, high thermal conductivity for faster cooling, wear and corrosion resistance, high yield strength properties are needs to be merged in a single structure. Nickel based alloys, especially Inconel 718, holds excellent mechanical properties such as high tensile, creep, fatigue and rupture strength on high temperatures and are widely used in aerospace industry [17]. Recently, the copper alloys have been started to be used in rocket propulsion to increase material efficiency with their excellent thermal conductivity. In regeneratively cooled rocket engines, GRCop-84 is utilized as the nozzle liner material [18,19]. Similarly, CuSn10 also stands for being a promising material in applications of cooling channels, fusion reactors, aviation industries due to its high heat conduction feature and wear resistance [20].

Additive manufacturing (AM) enables to manufacturing of multi-material structures in a post processing free state [21-23]. Especially, one of the additive manufacturing methods, directed energy deposition (DED) not only can fuse two different metals but also can produce functionally graded materials. In DED, metal powder melted by a laser are simultaneously deposited through a co-axial nozzle along the melt pool [24]. This method is easily adapted to manufacture FGM structures, since two or more powder hoppers can feed two or more material powder in DED. By doing so, compositionally graded structures can be manufactured since one can change the powder composition between layers [25,26]. Another advantage of the DED, the process provides a unique heterogeneous structure where the mechanical and thermal properties of the part vary throughout the structure itself to withstand severe environmental conditions in multiple directions [27]. However, undesired intermetallic phases in the microstructure still are a side product of the DED process since it is essentially a fusion process. This issue is widely witnessed phenomenon in different metal combining processes and attempted to

be addressed by several scholars [28-31]. The focus for these studies has been process optimization to increase mechanical and microstructural properties of the bimetallic structures. In the literature, there haven't been any studies that investigated the relation between thermodynamic modeling of the structure and experimental results to determine process parameters. By using the optimum DED parameters, one can achieve different mechanical properties along the structure according to the build. Thus, DED process is used for creating FGM CuSn10-IN718 for this study.

For FGM structures, understanding the relation between the process parameters and the microstructural behavior in the transition areas hold a great deal of importance. For the transition areas between two materials, the most problematic defections happen in fully mixed region. That's why in this study, 50%-50% CuSn10-Inconel718 FGM is produced by using DED method. Process parameters for FGM structure is developed whereas the microstructure, phase composition, elemental composition have been investigated with scanning electron microscopy (SEM) and energy dispersive spectroscopy (EDS). There has been few research work in the literature rely on experimental studies to determine optimum process parameters. However, to the best of our knowledge, there is a lack of study in the literature combining both experimental and thermochemical modeling work. In this study, an innovative approach has been used where the confirmation of thermodynamic calculations, CALculation of PHAse Diagrams (CALPHAD) modeling has been done via experimental work. Phases in the gradient zone has been compared with the data gathered from the CALPHAD to predict and verify experimental results with the thermodynamic studies.

2. LITERATURE REVIEW

2.1. Additive Manufacturing

Additive manufacturing is a unique manufacturing process that is capable of fabricating complex structures by adding one layer of related material on top of the previous one. This manufacturing method utilizes computer-aided design (CAD) data to produce structures by depositing material [32]. The traditional manufacturing methods generally operates by subtracting the material from a bulk structure, on the contrary in additive manufacturing, to produce a structure, very small thickness material layer added on top of each other. Fig 1. Shows additive manufacturing process steps for directed energy deposition (DED) and selective laser melting method (SLM)

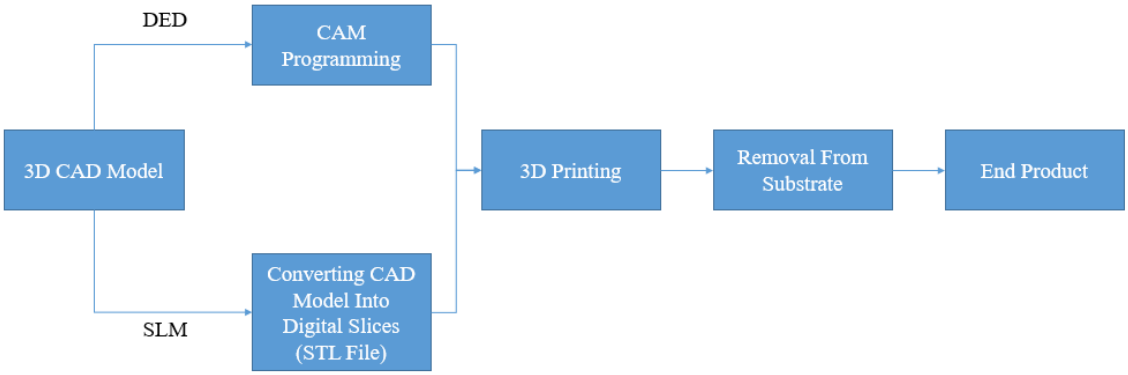

Figure 1 Additive Manufacturing Process Steps

2.2. Functionally Graded Materials

The need of a structure with various material properties to withstand specific working environments has been increasing in high technology applications such as the aerospace and nuclear sector [33,34]. To answer these needs from the industry, functionally graded materials (FGMs) have been started to be utilized. The composition of materials in FGM structures can be changed according to specific operational requirements which can lead to acquiring combined material properties from different materials in a single structure. To be able to avoid material failures like delamination and cracks, FGM structures need to be engineered to have smooth transitions [35].

2.3. Additive Manufacturing Methods for Functionally Graded Materials

It is essential to acknowledge that choosing right manufacturing method is crucial for FGM structures since it affects achieving desired results within microstructure and composition. As a conventional manufacturing method for FGMs there are a few research related to powder metallurgy (PM) techniques. PM technique is basically produces FGM structures by applying spatial distribution of constitutive materials followed by sintering to acquire fully consolidated structure [36]. Although such manufacturing method brings pore defection within the structure which leads to decrease in mechanical, thermal, physical, wear, corrosion properties [37]. With the problems coming from the FGM manufacturing with conventional methods, improved AM techniques drew attention of many scholars.

Additive manufacturing considered to be a freeform fabrication technology, which produces 3D metallic or non-metallic objects according to a digital model without a need of a mold [38]. In recent years, additive manufacturing methods are proposed for manufacturing FGMs with optimized mechanical properties. By the nature of AM, one can adjust the building orientation and process parameters to increase the mechanical integrity and produce complex objects which are impossible to produce with conventional

manufacturing methods such as machining [39,43]. Several additive manufacturing methods has been explained in the following sections.

2.3.1 Laser-based additive manufacturing methods

Two major and acknowledged laser-based metal AM methods are laser powder bed fusion (PBF) and directed energy deposition (DED) which are shown in Fig. 2a and b, respectively [44]. To be able to manufacture a structure with PBF method, first the geometry needs to be sliced to layers by using a slicing software, after that the part is produced layer by layer melting the related layer on top of the respective one using a focused laser heat source. It should be noted that there is no mold requirement for such manufacturing method. Throughout the LPBF, metal powders are heated so quickly to the melting state with the aid of a high-power laser, quenching with prefabricated structure leads to rapid solidification thus dense parts can be manufactured with integrated microstructure properties [47,48]. There are two types of PBF methods which are selective laser melting (SLM) and electron beam melting (EBM) [38].

The biggest difference between DED and LPBF is that DED utilizes a powder or wire feeding system instead of the powder bed. With the aid of a high-power laser, the metal powders are melted deposited on top of the substrate. Types of DED vary as laser engineered net shaping (LENS)-laser metal deposition (LMD), electron-beam free form fabrication (EBFFF) and wire arc additive manufacturing (WAAM). Capability of producing functionally graded materials is possible for every DED based AM process. PBF method is capable of producing more complex parts since such method has the advantage of manufacturability of high resolution and high surface quality compared to DED manufacturing processes. However, PBF methods are not commonly used for FGM structures since PBF method contains only single powder material in the powder chamber and it is very hard and nearly impossible to change the metal powder type during the manufacturing process. However, this method is capable of manufacturing gradient structures with pre-mixing powders or adjusting the porosity levels [52-54]. On the contrary DED-based additive manufacturing processes are considered throughout the literature to be more flexible and reliable to manufacture gradient structures since in these

processes powder feed and type can be controllable during the manufacturing process, one can adjust the composition of the structure by changing powder feed parameters. Also, it is possible to adjust the process parameters during the build thus complex gradient structures with better mechanical properties can be manufactured [55].

The gradient structure additive manufacturing schematic can be seen in Fig.3a. Generally, material selection for FGM structures is based on the engineering problem. According to the problem, material selections need to be done by taking into account of differences between mechanical, thermal, metallurgical properties. If there is a massive difference between selected materials, there can be delamination, crack and formation of undesired compounds according to these differences. In Fig. 3b-g, various building strategies can be seen for FGM structures. Linear gradient from %100 alloy A to %100 alloy B can be seen in Fig. 3b, for such strategy changing in composition is adjusted by the powder distribution capability of the AM process. Fig. 4c shows an FGM structure which can be called bimetallic structure. For such strategy, the transition area holds great importance to avoid delamination, crack problems. To overcome these issues, it is very common to use another 3rd material with mechanical-thermal properties are near to the mixed materials to ease the bonding behavior. In Fig. 3d, numerous gradients for single section created by using thermal expansion between two consecutive layer or by using magnetic property differences. Fig 3e. display a FGM structure that consists of three different materials, such build method is very essential to build two non-gradable material by introducing third intermediate material. In Figs. 3f and g, two different FGM structure has been shown. In the first schematic, due to process which obtained by a low heat energy, the strengthening phase particles were not dissolved fully in the construct. In the second schematic, one can see that strengthening obtained by secondary phases in the construct. In the FGM manufacturing with desired AM methods, it is essential to develop and determine the optimum process parameters such as laser power, powder feed rate, hatching distance, scanning speed to obtain a structure with desired mechanical properties. It is also important to characterize the end-product FGM to investigate and evaluate the microstructure, phase distribution, chemical composition, mechanical properties, thermal properties, corrosion and wear resistance properties to be able to improve the repeatability and ensure a successful fabrication of gradient material [56].

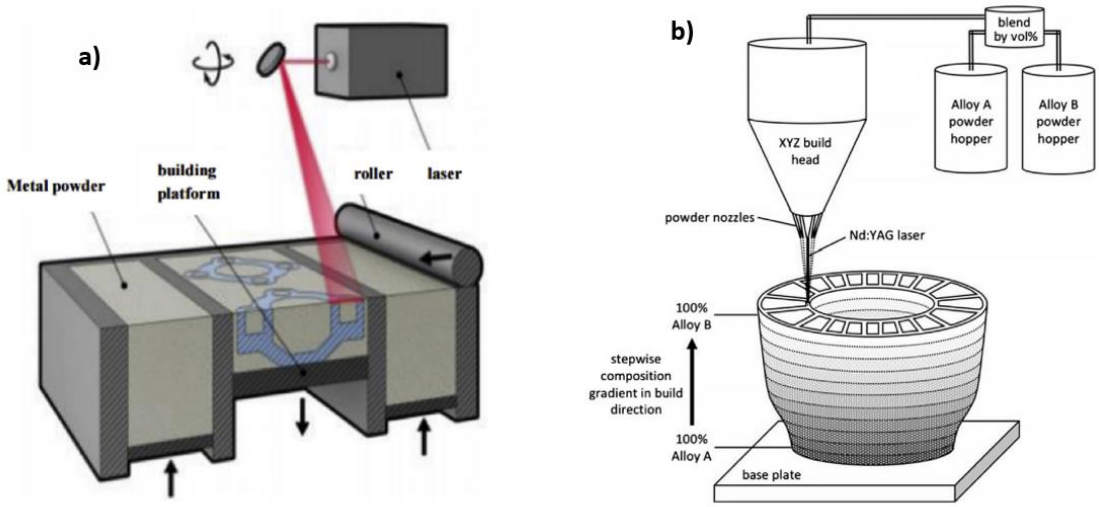

Figure 2 (a) LPBF process demonstration [45] (b) DED process demonstration [46].

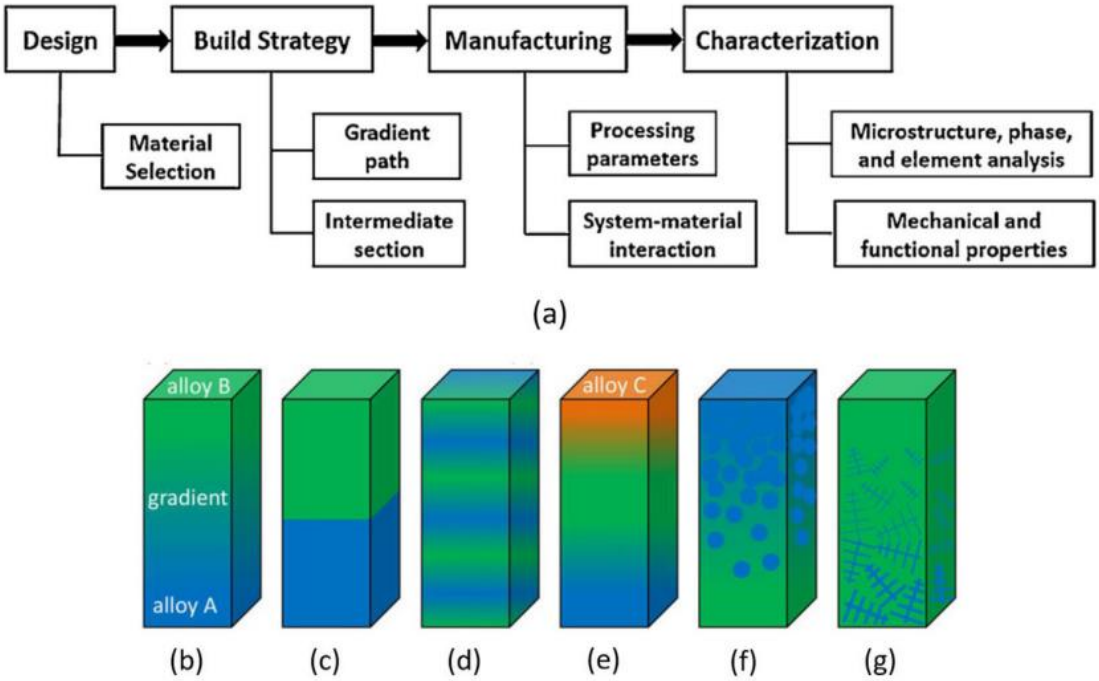

Figure 3 Schematic of gradient structure manufacturing by DED process [57]. b-g) Demonstration of various deposition examples for FGM structures [58]

2.4. Challenges and Possible Solutions Related FGM Manufacturing with Metal AM Technology

The metallic FGM manufacturing process still needs comprehensive research and understanding of process & material property relationship. Various challenges and possible solutions are discussed as follows for DED method.

2.4.1. Incongruity Between Alloys

In DED, each material possesses different melting points, such property affects the heat input values for that specific material to be optimally melted. Thus, when mixing different materials considered, the effectiveness of heat input value changes since there are various influencers comes into the process. This could cause overheating of some elements with a lower melting point [59]. Additionally, segregation, porosity, dimensional and non-melted sections defects can be seen in the structure which is caused by difference in density and liquid surface tension between two different materials [60]. Moreover, crack formation can begin due to differences in coefficient of thermal expansion, crystal structure and elastic modulus differences. Incompatibility and insolubility are two big problems in FGM manufacturing through metal additive manufacturing methods, since such problems leads to brittle phases (intermetallic components). With residual stress inherent in process, the brittle phases cannot withstand such stress and leads to crack formation and affects mechanical properties severely. In Fig 4, delamination and crack problems can be seen. Additionally, it is important to keep in mind that reaction of thermal energy for materials varies, for real life application such property needs to be determined for mechanical integrity of the end product.

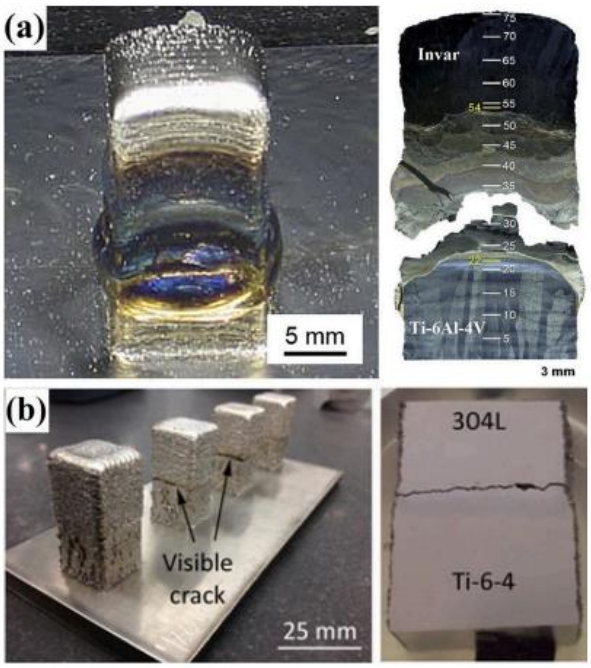

Figure 4 Failure examples of dissimilar bimetalic gradient structures; (a) Ti-6Al-4 V to Invar [61], and (b) Ti-6Al-4 V to V to 304 L [58].

Copper based FG structures encounter big challenges due to the low absorptivity of copper. Additionally, when copper alloy mixed with iron, the limited solubility of iron and copper causes another major problem since thermomechanical properties for these materials are very different. Because of these reasons many trials for copper-iron functionally graded structures ended up with segregation problems.

Nonconforming process parameters in DED process could lead to unmelted regions, microcracks and porosity observed in trials of fabrication H13 tool steel on copper substrate [62]. In another study, a pre-mixture of H13/Cu powders with 50 % Cu approach was utilized for LPBF method. The results showed cracks and porosity in the manufactured parts [63]. H13 steel to copper study is investigated by Noecker and DuPont et al. by splitting cracking in three ranges as low, medium, and high. They have founded that crack occurs in a range of 11.5-50 wt. %Cu within the gradient [64]. To obtain crack-free FGM structures with H13 to copper, Articek et al. (2013) altered the material composition by 10 wt.% for every 10 layers. With this strategy, low porosity levels were observed. Additionally, the tensile and microhardness improvements were examined in the end-product [65]. Another study is executed by Bonny Onuike et al. (2018) to bring together GrCop84 and Inconel 718 by using the LENS system. Initial trials ended up with

bonding and diffusion problems which can be seen in Fig 5. The thermal absorptivity and thermal conductivity differences between dissimilar materials brough in some major problems. To obtain a successful structure, the researchers introduced a compositional layer between two materials. The microstructural investigations showed successful deposition of GRcop84-Inconel 718 bimetallic structures. Microstructural investigations show that, Cr2Nb precipitates occurred in the transition areas. According to the results, there was an increase in hardness profile as well [66].

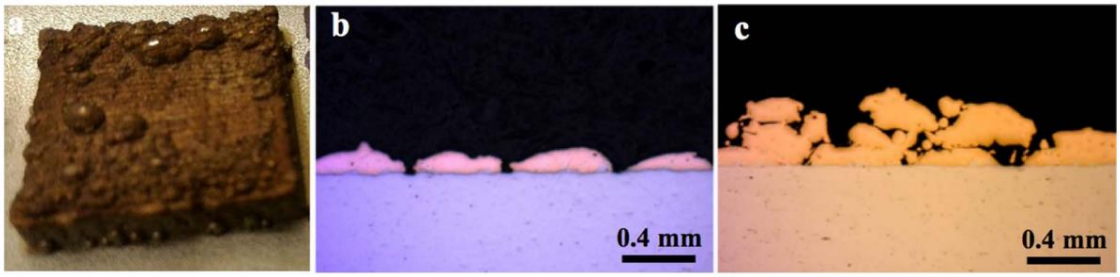

Figure 5 Failure images of GRCop-84 - Inconel 718 FGM deposition: (a) As built sample, (b) bonding and diffusion problems GRCop-84 on Inconel 718, and (c) GRCop-84 - Inconel 718 bonding problems [66].

2.4.2. Process Modelling

As an effective tool, process modeling is utilized to predict and to control the microstructural properties for FGM manufacturing. Nevertheless, different material properties, lack of data on thermomechanical properties makes process modeling harder since the compositions are temperature dependent. Additionally, there is a continuous change in the compositions because of adding different materials/alloys which affects the melt pool in DED processes. Thus, to be able to predict the thermomechanical properties of the FGM, the data can be evaluated into a polynomial for all materials. Other option is to use complex thermodynamic modeling programs to predict thermomechanical properties [67].

In the literature, the investigations are focused on the characterization of different FGM structures manufactured with AM technology. In voxel-based path plan developed by Yan

et al. (2018) [68], each voxel is determined by the relation with position, process parameters, and composition. Muller et al. (2013,2014) studied both spiral and zigzag tool-path strategies to define these tool path effects on the performance for manufacturing of FGM parts with DED as can be seen from Fig 6. [69,70]. Process control predictions to be able to control the feed with delays for more accurate and repeatable builds proposed by these researchers. Path planning is validated through performance integers. Nevertheless, the path planning with high variance values ended up with high inaccuracy.

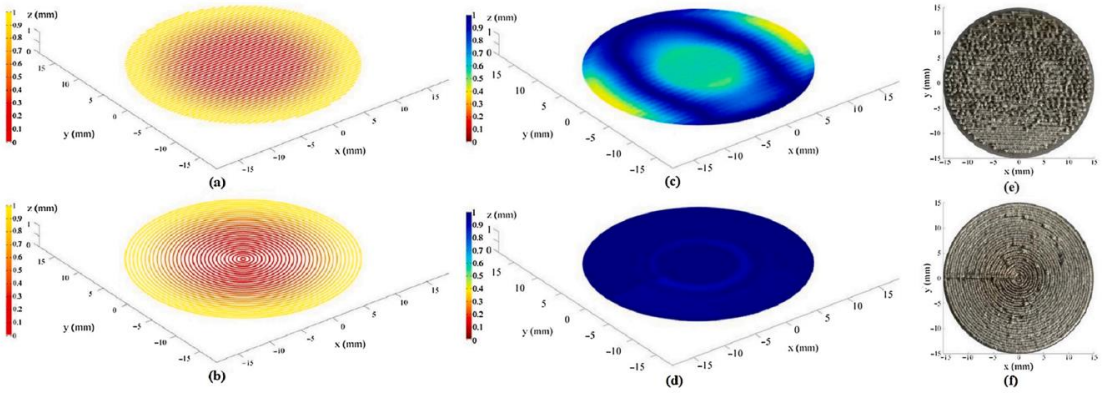

Figure 6 Simulation of toolpath strategies of (a,c,e) zigzag, (b,d,f) spiral [69]

2.4.3. Thermochemical Modelling Approach

To be able to predict undesired brittle phases, multicomponent phase diagram development by thermochemical modeling is utilized by many researchers. It gives an insight on the phase transformations and thermomechanical properties of the manufactured part. Such approach can be utilized for equilibrium or non-equilibrium processes, although applying the identical thermal history of manufacturing process is near impossible so prediction of a non-equilibrium process like DED may not be precise. However, thermochemical modeling can determine whether it is feasible or not to manufacture specific FGM. To achieve desired gradient material, multicomponent phase diagrams are useful as guiding maps. The CALPHAD (CALculation of PHAse Diagrams) is generally utilized for thermochemical modeling. In the literature, CALPHAD approach was performed by few studies to investigate the forming of the

phases under equilibrium or nonequilibrium conditions for FGMs. For example, Carroll et al. evaluated the experimental results that they gathered from the SS304L-Inconel625 FGM gradient zone with phase fraction calculations in order to show the inclination to precipitate undesired phases on the gradient zones [71]. In order to investigate secondary phases in Ti6Al4V-Invar36 FGM structure, Bobbio et al. applied equilibrium calculations [61]. Similar approaches have been conducted in [35,72,73]. As another example, Li et al. used room temperatures in equilibrium and nonequilibrium calculations in order to exhibit forming phases in Fe-Cr-Ni gradient structures [74].

3. EXPERIMENTAL STUDY AND THERMOCHEMICAL MODELLING

The work presented here includes submitted work to the journal of Additive Manufacturing Technologies and unpublished results.

By combining low-cost high thermal conductivity copper alloy with high strength corrosion resistant nickel alloy, the desired thermomechanical properties can be achieved for various applications in aerospace and others. This motived us to use two aerospace materials Inconel 718 and CuSn10 for this study.

The gradient material is fabricated via DMG Mori Seiki LASERTEC 65 DED Hybrid machine which is utilizing directed energy deposition manufacturing method. This system uses a 2.5kW diode laser, 735 mm x 650 mm x 560 mm working area, double hoppers and can deposit material up to feed rate of 1 kg/h. By the help of coaxial nozzle, evenly distribution of metal powders becomes possible. The system can be seen in Figure 7.

Figure 7 DMG Mori Seiki LASERTEC 65 DED Hybrid [75]

In 718 powder (Oerlikon, Freienbach, Switzerland) with a particle size ranging between 106 - 45 µm and CuSn10 powder (Schlenk, Roth, Germany) with a mesh size of 63 - 160 µm has been used as metal powders to fabricate FGM structures on a C45 type Carbon steel substrate. The chemical compositions of the metal powders are given in Table 1.

Table 1: Metal powder chemical compositions in weight percent

	Inconel 718	CuSn10
Ni	53.9	-
Cr	18	-
Fe	18	-
Nb	5	-
Mo	3	-
Al	0.6	-
Ti	1	-
Cu	-	90
Sn		10
P		0.07

A high-powered fiber-coupled diode laser creates a melt pool on which metal powder is deposited directly into. Whole manufacturing process was executed under argon shielding and carrier gas. The two different hoppers simultaneously deliver the multiple metal powders, and thereby enable the fabrication of multi-material structures.

3.1. Computer Aided Manufacturing (CAM)

To be able to produce any designed parts, computer aided manufacturing (CAM) is needed. CAM is essentially an application which utilizes computer software to produce computer numerical control (CNC) programs for subtractive or additive manufacturing methods. Siemens NX CAD/CAM module has been used to develop additive programming which is fully integrated with LASERTEC 65 DED system.

In order to begin the CAM programming, a digital copy of the system needs to be defined in the NX. To be able to simulate the fabricating process and make sure that there is no collision throughout the manufacturing process, the machine, laserhead, fixture and laser tool needs to be identified as can be seen from Fig 8.

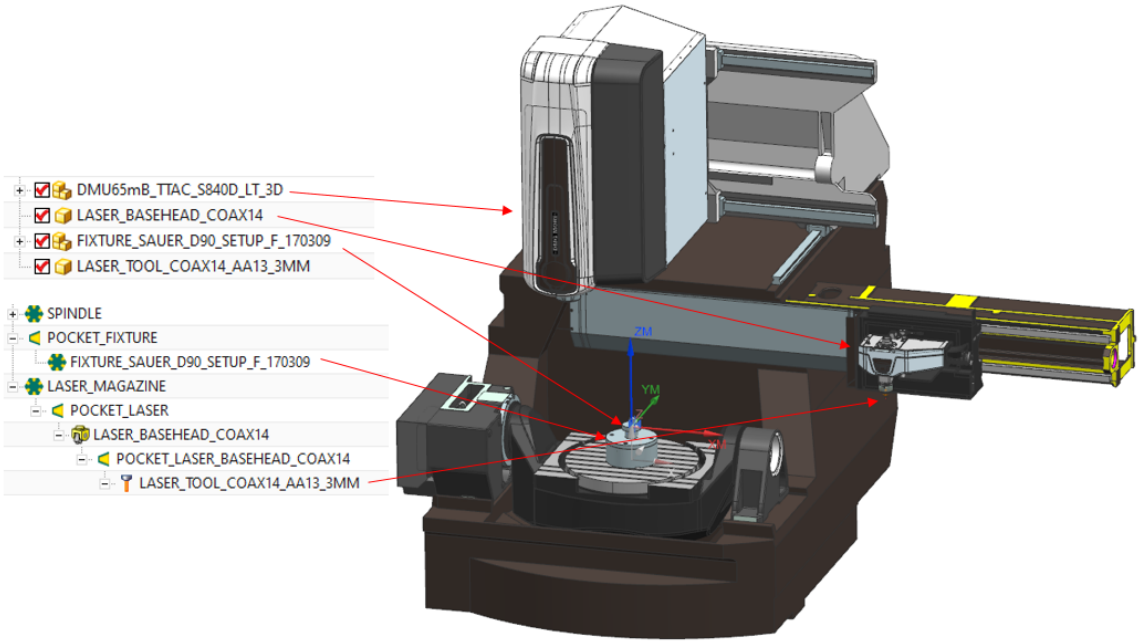

Figure 8 Digital copy of LASERTEC 65 DED system

After the identification of the system, fabrication strategy needs to be defined. In our study we used planar additive profile with zigzag infill method which is recommended for rectangular shapes. Then CAD model of the desired product needs to be selected as additive structure and foundation face needs to be identified as well as can be seen from Fig 9.

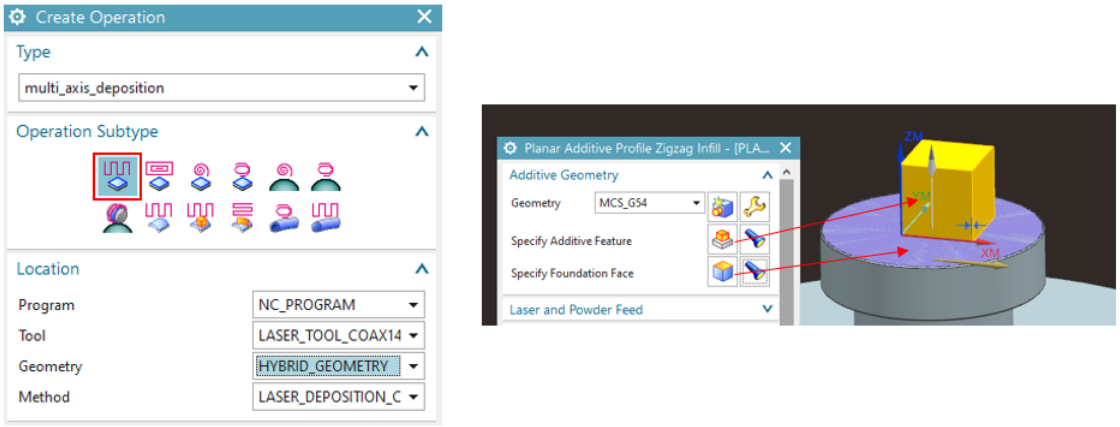

Figure 9 Identification of additive structure and foundation face

Process parameters such as laser power, hatch distance, scan speed and layer thickness need to be set in the program before fabrication process as shown in Fig. 10.

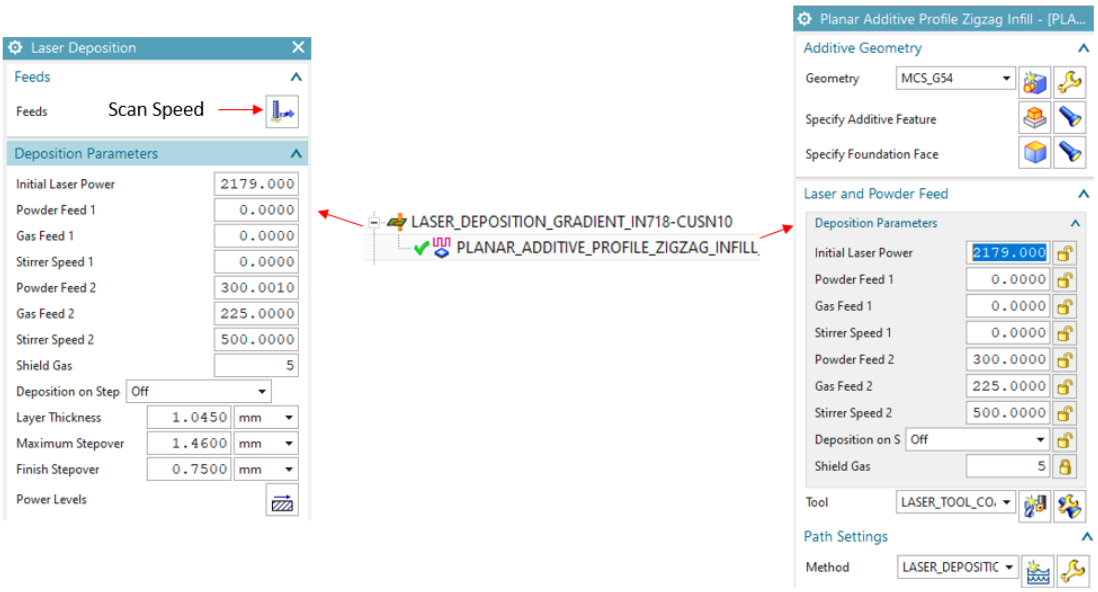

Figure 10 Process parameter identification

After the parameter adjustments, simulating the manufacturing process and verification of the additive operation is necessary to evaluate the fabrication process, movement of the tool and detect if there is any collision risk (in Fig. 11). When evaluation is finished then it is safe to send the G-Code of the program to the machine.

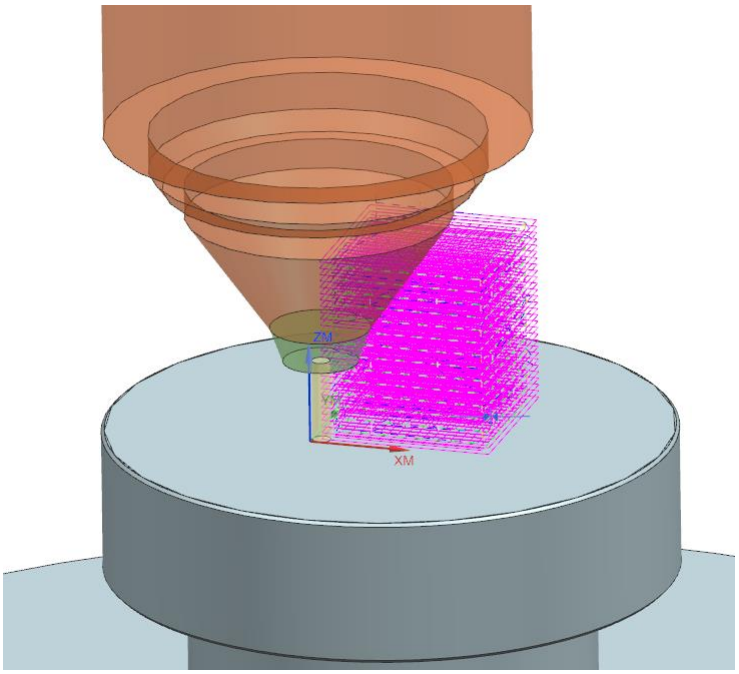

Figure 11 Deposition assessment through CAM program

3.2. Process Parameters Development

To produce high quality structures, optimizing the main process parameters such as laser power, scan speed, hatch distance, powder flow rate, and layer thickness is required. Moreover, the dissimilarity between the thermal properties of multi-material structures is an aspect that needs to be taken into account. These intrinsic properties are the heat capacity, melting point, and coefficient of linear thermal expansion in different materials. Here, the FGM material process parameters development is started by 50%-50% Inconel 718-CuSn10 single-track trials. To determine the starting parameters set, a variant of the total energy input per volume (E) equation is used. Total energy input equation (3.1) contains the laser power (P), scan speed (v), layer thickness (h), and hatch distance (t),

since these are the parameters that have the greatest impact on the energy density. The total energy input unit is J/mm^3 [76,77].

$$E = \frac{P}{v * h * t} \tag{3.1}$$

For single track trials, hatch distance parameter becomes irrelevant and by removing the hatch distance from the equation, energy input per area is used to obtain initial process parameters. Energy input per area unit is J/mm^2.

$$E = \frac{P}{v * h} \tag{3.2}$$

Prior to manufacturing IN-718/CuSn10 FGM, we have optimized the process parameters for IN 718 and CuSn10 separately with experimental studies given below.

3.2.1. Optimizing CuSn10 and In718 Process Parameters

Optimizing the process parameters for single materials holds big importance to understand the response behavior of the materials to different energy input values. Especially fabrication of copper has many challenges due to its massive reflectivity and energy absorption properties. Furthermore, copper can dissipate the heat so fast because of its high thermal conductivity which can lead to unstable melt pool behavior [78,79]. Initial trial parameter values have been gathered from literature to calculate initial total energy input trial values. Experimental work was conducted with various total energy input values until optimization is complete. There were various failures until the optimized structures were achieved which can be seen from Fig. 12. Reasons for these failures vary, some of them failed due to overheating, which is caused by high total energy input while some failed due to high scanning speed which leads to insufficient bonding between layers.

Figure 12 Failed CuSn10 trials due to overheat and overdeposition

It has been observed that the CuSn10 cubic trials with total energy input value between 100 J/mm^3 and 200 J/mm^3 gave promising results since there was no insufficient bonding, dilution, overheat and large defections on the structures. Thus, on these trial samples, microstructure investigation has been conducted to examine the porosity levels to decide the optimized process parameters. Process parameters for these CuSn10 trials have been given in Table 2. There are several reasons for porosity to occur in a structure, one of them is utilizing high energy input during fabrication which leads dents and holes [80]. Since porosity negatively affect the mechanical properties such as fatigue resistance and could cause crack propagation, the porosity measurement is considered to be the initial main quality check test for additively manufactured parts.

Table 2: 15 mm -15 mm – 20 mm CuSn10 cubic trials

	Laser power (J/s)	Scan Speed (mm/s)	Hatch distance (mm)	Layer thickness (mm)	Total energy input per volume (j/mm^3)
CuSn10 Cubic 1	1800	7	1.35	0.97	196.367
CuSn10 Cubic 2	2000	12.50	1.35	0.97	122.184
CuSn10 Cubic 3	2400	12.50	1.35	0.97	146.620

Fig.13 shows the Eclipse LV100ND (NIKON) which is used for porosity investigations. The micrograph images taken from the build direction cross-section of CuSn10 structures can be seen in Fig. 14-16.

Figure 13 Eclipse LV100ND (NIKON) [81]

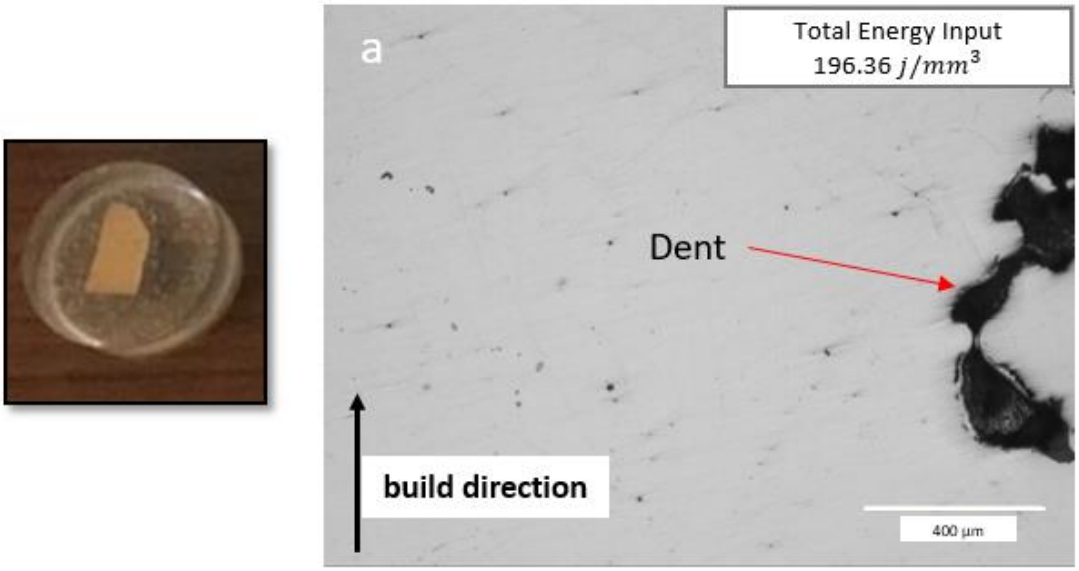

Figure 14 Micrograph images of CuSn10 fabricated with 196.36 j/mm^3 cross section results

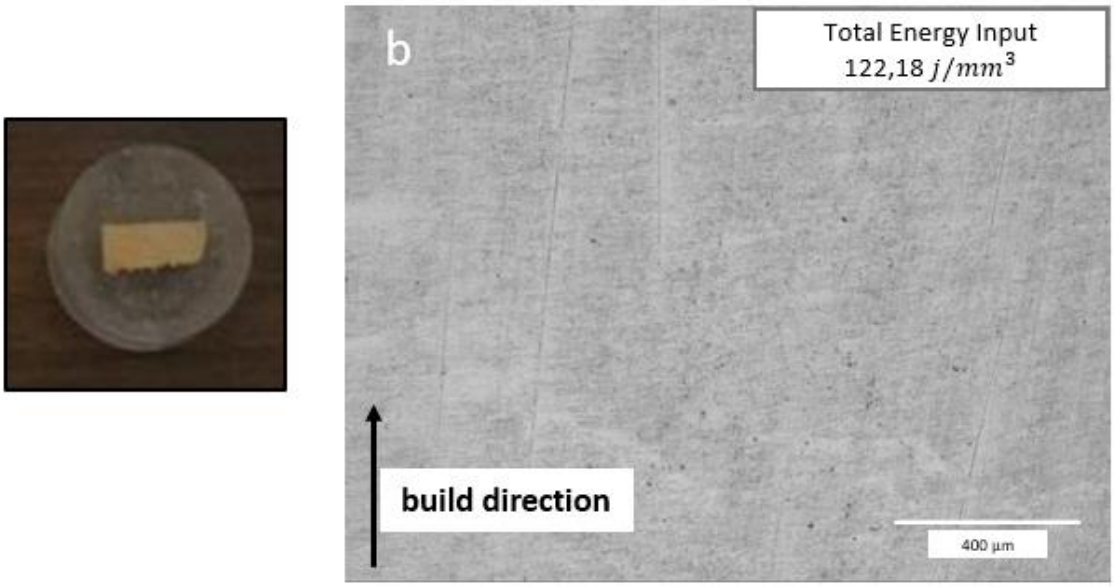

Figure 15 Micrograph image of CuSn10 fabricated with 122,18 j/mm^3 cross section results

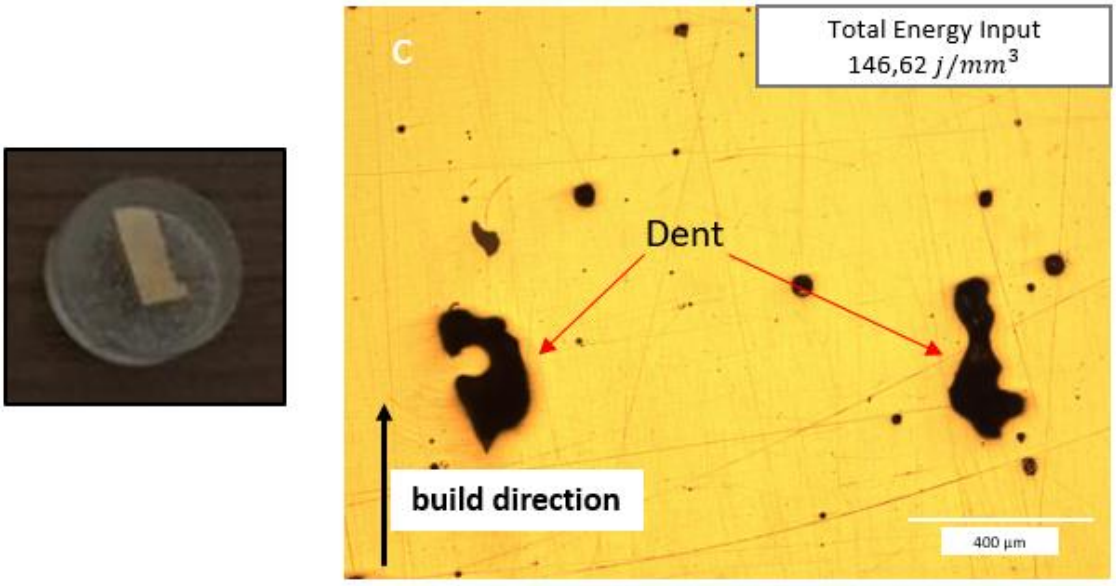

Figure 16 Micrograph image of CuSn10 fabricated with 146.62 j/mm^3 cross section results

Dents and clustered holes observed in the CuSn10 cubic 3 which is fabricated with 196.36 J/mm^3 total energy input. Also, the same defects were detected in the CuSn10 cubic 1

which is fabricated with 146.62 J/mm^3, additionally, this sample has pores that are close to each other which could lead to decrease in fatigue life. On the other hand, the CuSn10 cubic 2 fabricated with 122,18 J/mm^3 total energy input showed no dent and the porosity levels were minimum when compared to other trial cubic. Thus the cubic 2 with the best porosity results was selected as the optimized structure which is demonstrated in Fig 17.

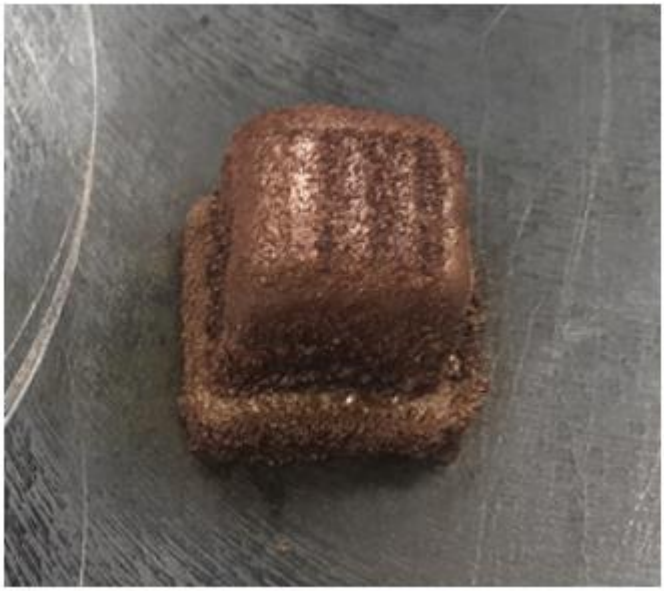

Figure 17 Optimized CuSn10 Structure

Table 3: Optimized DED process parameters of CuSn10

	Laser power (J/s)	Scan Speed (mm/s)	Hatch distance (mm)	Layer thickness (mm)	Total energy input per volume (j/mm^3)
CuSn10 Optimized Process Parameters	2000	12.5	1.35	0.97	122.18

Same procedures were executed for In718 optimization and 71.42 J/mm^3 selected as optimized total energy input. The optimized structure can be seen in Fig 18. The related process parameters to obtain such value is given in Table 4.

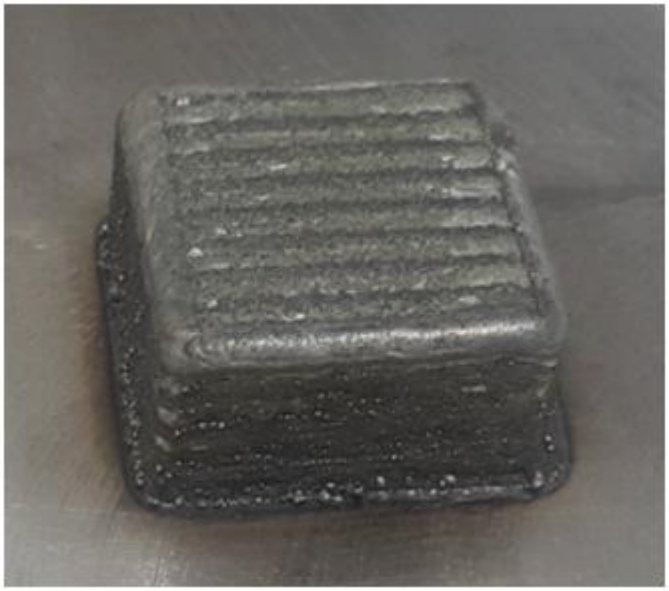

Figure 18 Optimized In718 Structure

Table 4: Optimized DED process parameters of In718

	Laser power (J/s)	Scan Speed (mm/s)	Hatch distance (mm)	Layer thickness (mm)	Total energy input per volume (j/mm^3)
In718 Optimized Process Parameters	2000	16.66	1.5	1.12	71.42

3.2.2 Optimizing CuSn10-In718 FGM Process Parameters

CuSn10-In718 FGM structure process parameter optimization started with single track trials. For initial energy per area value selection, these optimized single material process parameters such as laser power, layer thickness and scan speed are taken into account and calculated 107.14 j/mm^2 and 164.94 j/mm^2 respectively, for Inconel 718 and CuSn10 alloys. Thus 136.09 j/mm^2 is calculated to achieve a gradient structure and related process parameter values are selected to give the same total energy input per area. Then, by using different total energy input per area values and different powder feed for same total energy input nine single track structures have been manufactured to evaluate the structures and achieve the optimized single track. Figure 19 represents the nine single-

track trials using different laser power and powder feed parameters as demonstrated in Table 5. The reason for changing the powder feed parameter between single-track trials is to achieve a structure without steep edges.

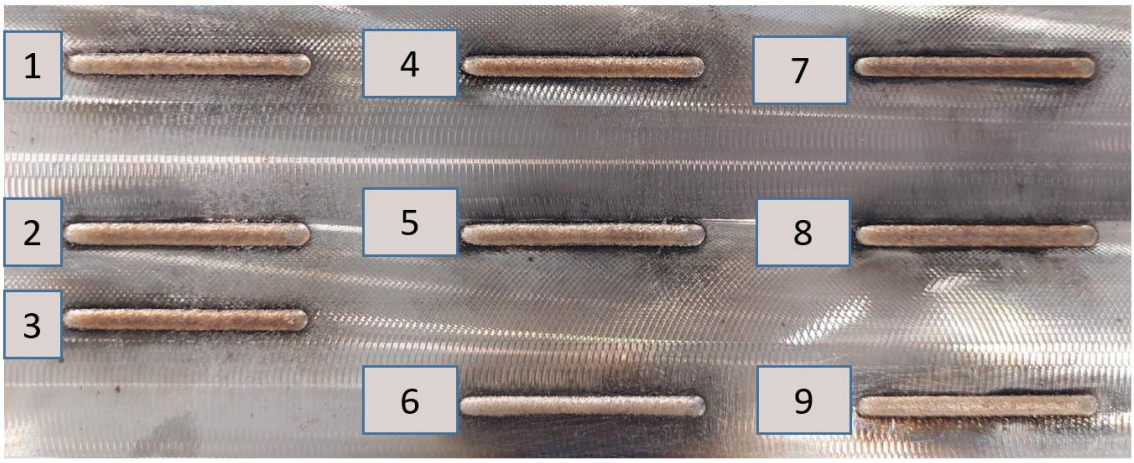

Figure 19 FGM Single track trials

Table 5: Single track trial process parameters

	Laser Power (Watt)	Layer Thickness (mm)	Scan Speed (mm/s)	Powder Feed (g/min)	Total Energy Input Per Area (j/mm^2)
No:1	1874	1,045	14,58	12,37	122,96
No:2	2274	1,045	14,58	12,37	149.21
No:3	2074	1,045	14,58	12,37	136,09
No:4	1874	1,045	14,58	15,77	122,96
No:5	2274	1,045	14,58	15,77	149.21
No:6	2074	1,045	14,58	15,77	136,09
No:7	1874	1,045	14,58	8,87	122,96
No:8	2274	1,045	14,58	8,87	149.21
No:9	2074	1,045	14,58	8,87	136,09

Fig. 20 represents the selected single track out of nine single track trials which are fabricated using different laser power and powder feed parameters. The best single track is selected by examining the specimens from the aspects of the bonding quality, and formation of delamination, dilution, and steep edges. Process parameters has been given in Table 6.

Figure 20 Optimized single track trial (No:5)

Table 6: Optimized process parameters for gradient single track

	Laser Power (J/s)	Layer Thickness (mm)	Scan Speed (mm/s)	Powder Feed (g/min)	Total Energy Input Per Area (j/mm^2)
No:5	2274	1,045	14,58	15,77	149.21

Laser power and powder feed parameters from the selected single-track structure are taken into account for 50%-50% Inconel 718-CuSn10 cubic structure, since material development process indicates to stabilize good bonding with the substrate first. However, the final laser power parameter for the cubic structure is changed due to achieve a gradient structure with better mechanical integrity. For such optimization, calculated total energy input per volume for the single material optimization of Inconel 718 and CuSn10 are used as 71.42 j/mm^3 and 122.18 j/mm^3, respectively. After a comprehensive experimental study, the optimized total energy input for CuSn10-In718

FGM structure is achieved as 97.93 j/mm^3. The related optimized process parameters are given in Table 7.

Table 7: Optimized process parameters of gradient cubic structure

	Laser power (J/s)	Scan Speed (mm/s)	Hatch distance (mm)	Layer thickness (mm)	Total energy input per volume (j/mm^3)
CuSn10-In718 FGM Optimized Process Parameters	2179	14,58	1.46	1.045	97.93

Fig. 21a shows 3D view and Fig. 21b shows cross section view of 30mm x 30mm x 30mm Inconel 718-CuSn10 50%-50% graded structure that has been manufactured using the optimum DED process parameters. Microstructural investigation and evaluation are given in the results and discussion section.

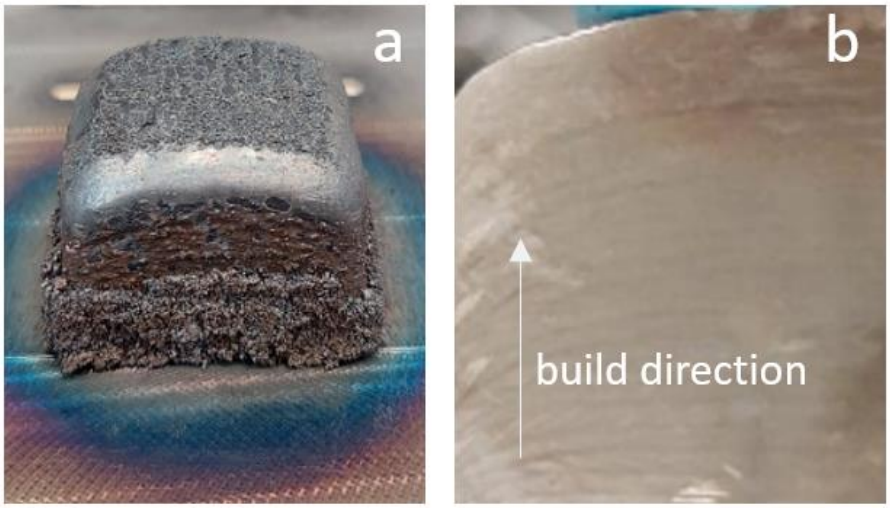

Figure 21 Inconel 718 – CuSn10 gradient structure: (a) optimized 30x30x30 mm cubic, (b) cross section view of cubic in build direction

3.3. Characterization of Inconel 718-CuSn10 Gradient Structure

The sample is removed from the substrate using automatic double column bandsaw machine (Kesmak KYS 400 x 600). The manufactured FGM sample was sectioned across the building axis to observe the cross-section of the specimen by using Discotom 10 (Struers) precision cutting machine demonstrated in Fig [22].

Figure 22 Struers Discotom 10 [82]

The cross-section was wet-polished using SiC grinding papers up to 4000 grit, then followed by cloth polishing using 1 μm aluminum-oxide suspension media. A solution containing 40% HCI (hydrochloric acid), 30% CH3COOH (acetic acid), and 30% HNO3 (nitric acid) was prepared for chemical etching of mirror-polished samples. Etching was then performed by the prepared chemical solution for 15 seconds to expose the microstructural features.

Subsequent to the polishing procedure, the gradient structure is examined with scanning electron microscope (SEM) by using field emission gun (FE-SEM, Zeiss Leo Supra VP 35) at 20kV accelerating voltage. Energy dispersive X-ray spectroscopy (EDX) (Oxford Instruments, Oxford, UK) was performed to generate elemental composition and evaluate the compositional variation as well as diffusion throughout the selected zones. Additionally X-Ray diffraction (XRD) was executed with Rigaku Ultima which utilizes a Cu source operating with 40 kV and 30mA.

Figure 23 Leo SUPRA 35VP FEG-SEM measurement device [83]

3.4. Thermodynamic Computation

Mechanical properties of alloys rely on the relative stability of ingredient phases. Thermodynamic analyses of such systems give a projection on the tendency of gradient alloys to precipitate undesirable phases during processing. To determine this tendency, equilibrium phase diagrams can be computed by using CALculation of PHAse Diagrams (CALPHAD) method [84,85]. In this work, we have used this approach to get an insight about the end products microstructure while optimizing the DED process parameters.

A CALPHAD model was performed by using “Equilib” module of FactSage™ 8.1 thermochemistry software [86] to predict the possible phases during equilibrium cooling of 50:50 mixture (by weight) of CuSn10:Inconel718 alloy from molten state. The thermodynamic data for the calculation was taken from FSstel solution database.

3.4.1. CALPHAD Approach

Calculation of phase diagrams (CALPHAD) is an approach which is modelling the Gibbs energies as a function of various parameters such as temperature, pressure, and composition in order to predict phase equilibria of unknown chemical reactions [87]. With CALPHAD it is possible to predict higher-order systems than ternary systems. Fig. 24 represents the CALPHAD approach.

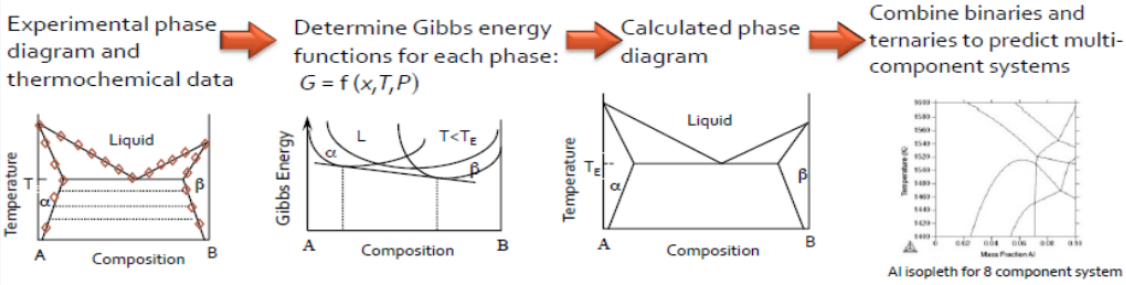

Figure 24 Schematic of CALPHAD Approach [88]

This is basically an approach which systematically calculates the multi component phase diagrams. The CALPHAD relies on the assumption that a phase diagram is a function of the equilibrium thermodynamic variables of the structure [87]. Applications like FactSAGE, Thermo-Calc, and PANDAT are software tools to apply CALPHAD method. Usage of multicomponent phase diagrams are advantageous for alloy development as well [31]. CALPHAD is also useful to determine the transition behavior from one metal alloy to another. In Fig. 25, various multicomponent phase diagrams for different gradient paths can be seen. Linear gradient path which includes direct mixture of one metal alloy to another is shown in Fig. 25a. When linear route faces undesired phases as can be seen in colored regions of Fig. 25b, the gradient path can be curved for that region. To reduce complexity, transitions through the system can be helpful. In Fig. 25c, a discontinuous gradient path can be seen along the blue line. It can be interpreted that the alloy tends to be graded to the closest pure metal in multicomponent phase diagrams, after that graded with another pure metal which is close to the selected alloy, then finally grading occurs with the targeted alloy [58].

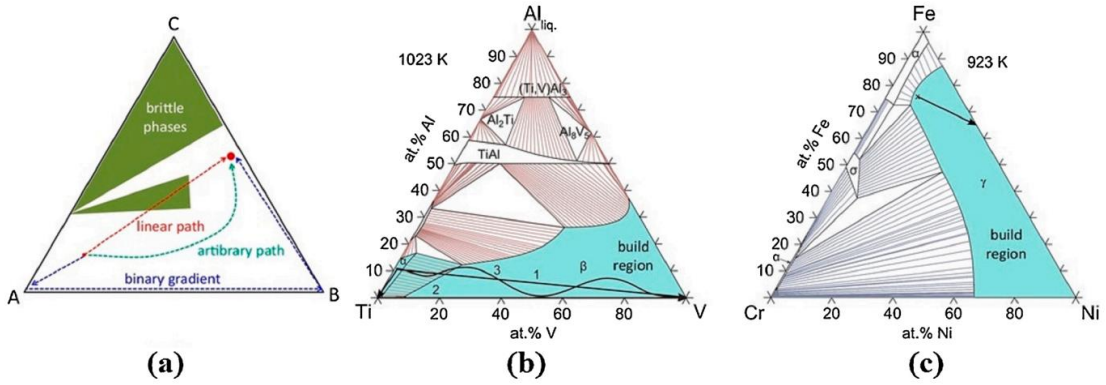

Figure 25 (a) Paths of possible gradients in a ternary phase. (b) Al–Ti–V (c) Fe–Ni–Cr phase diagrams demonstrating absence of brittle phases in gradient paths (58)

3.4.2. Scheil Solidification Model

One can describe a solidification model with lever rule where solvated atoms in solid and liquid presumed to succeed full rapid diffusion so that solution stays homogeneous [89]. For additive manufacturing processes, such approach is not feasible to use since AM processes inherit massive cooling rates due to the nature of the process. For example, DED cooling rate is over $10^3 K/s$ [90]. Thus lever-rule cannot be applied under this environment. In the literature, Scheil model is utilized for AM processes since this model assumes no solute in the solid-state while assuming infinite fast solute diffusion in liquid state. At the liquid-solid interface, a thermodynamic equilibrium is assumed for this approach and following equations are used to be able to determine the equilibrium concentration of solid at the interface [91].

$$C_s = kC_0(1 - f_s)^{k-1} \tag{3.3}$$

$$k = \frac{C_s}{C_l} \tag{3.4}$$

Solid composition defined as C_s is the where C_l represent liquid composition on the interface, alloy composition at initial point is C_0 while local equilibrium partition coefficient is k which is derived from the ratio of C_s and C_l. f_s represents the fraction of the solid phase.

4. RESULTS AND DISCUSSION

The microstructural investigations shows that the gradient structure without any defects has been successfully fabricated. Both Inconel 718 and CuSn10 having the same unit cells as face centered cubic, improved the compatibility and the natural transition between two alloys is achieved. SEM images have been given in Fig. 26, captured from three different regions with 5 mm interval along the build direction.

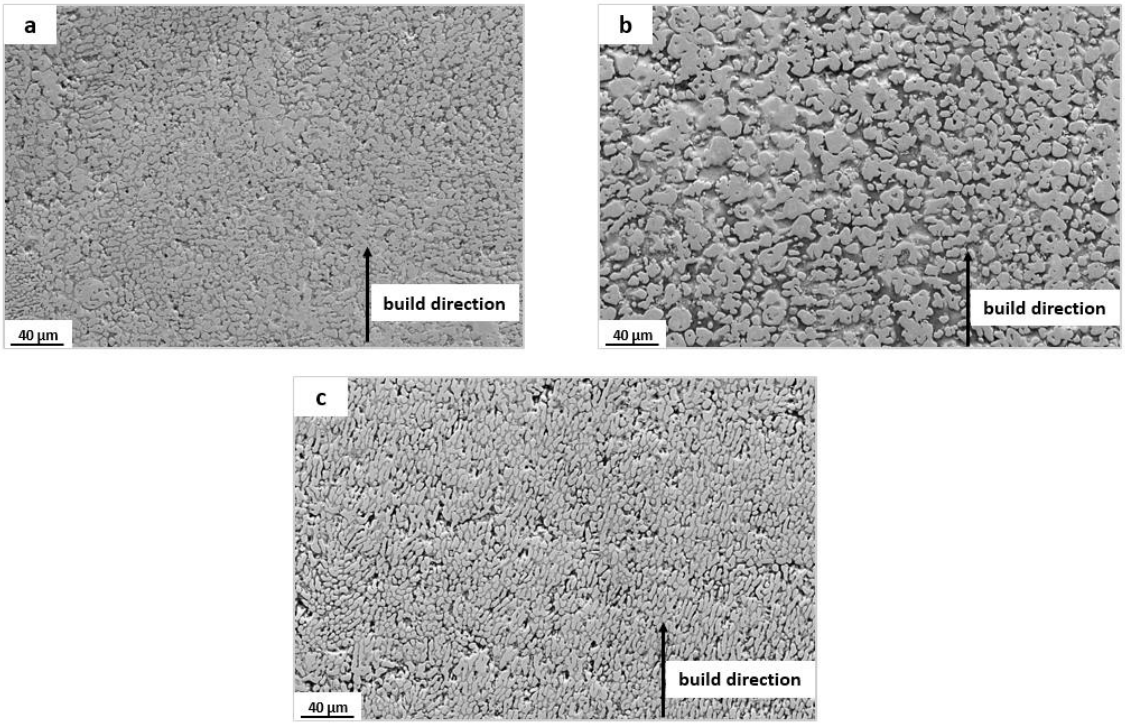

Figure 26 SEM images of gradient structure from three different regions with 5 mm interval along build direction

In (Fig. 26a-c) gradient zones, equiaxed and columnar structures were detected with a continuous distribution, which might help to form the good metallurgical bond throughout

the structure [92]. The equiaxed structure in Fig. 26b displays a coarser grain size when compared to the Fig. 26a and c. This microstructure difference throughout the build direction might be explained with the ratio of temperature gradient (G) to solidification velocity (V) along the manufacturing process since G/V plays important role on the form of the microstructure [93]. Decrease in G/V changes microstructure towards equiaxed dendritic structure from a columnar dendritic structure [94]. This effect originates from the variance on G/V throughout the build direction. The related studies have stated that G/V possesses the highest value at the very beginning of the manufacturing process when first layers are deposited [94]. The reason behind this is that high heat conduction to the substrate occurs at the beginning of the deposition process since the substrate's initial temperature was at the room temperature. As a result, the alignment between direction of the heat flow and build direction originates which causes forming of columnar dendrites. As layers added along the build direction, the ratio of temperature gradient to solidification velocity decreases. As deposition continues, the substrate temperature increases which causes to temperature gradient decrease since temperature difference between consecutive layers reduced. This leads to microstructure change to equiaxed structure from columnar dendrites [95]. This behavior is very similar to our findings since there is a 5 mm interval and it can be seen that microstructure changes towards equiaxed structure as shown in Fig. 26c to Fig. 26b.

During the manufacturing process, the FGM sample was rotated 90° between consecutive layers, which means 90° hatch angle parameter utilized. It is stated that direction of the laser indicates the columnar dendrite growth direction [97]. This proves that the observed dendrite structures on the examined gradient zones are disordered while incessant between layers. In general, the microstructure displays adjoined properties across the build direction of the gradient zone. In this study, we have observed a dendritic structure in CuSn10 and In718 FGM material similar to studies of C. Shang, et al. and S. Scudino et al. [92,97]

Formation of microstructure during directed energy deposition is heavily affected by the cooling rate of consecutive layer. Amine et al. stated that by combining high laser power with low scan speed, slow cooling rates achieved while low laser power and high scan speed results in high cooling rates in DED [98]. It is known that DED possesses high cooling rates which leads to dendrite structures in microstructural behavior. Liverani et

al. stated that the effect of process parameters on the cooling rates directly results in changes in microstructure [99].

Several zones were selected through the build direction randomly and EDS area mapping was conducted. It is concluded that the elemental composition across the gradient zone follows the designed composition without a major divergence. Fig. 27 shows the related elemental composition through a randomly selected zone. The designed composition and the actual composition measured by EDS (weight percent average of EDS area mapping zones) are tabulated in Fig. 27b, presenting that the planned composition for the gradient structure is nearly the same as the experimentally obtained one. The error percentage between designed and achieved composition can be justified by the limitations of the EDS process [100]. (Fig. 27 c-h) demonstrates homogenous gradient structure with evenly distributed Ni, Cu, Cr, Fe, Sn, Nb elements.

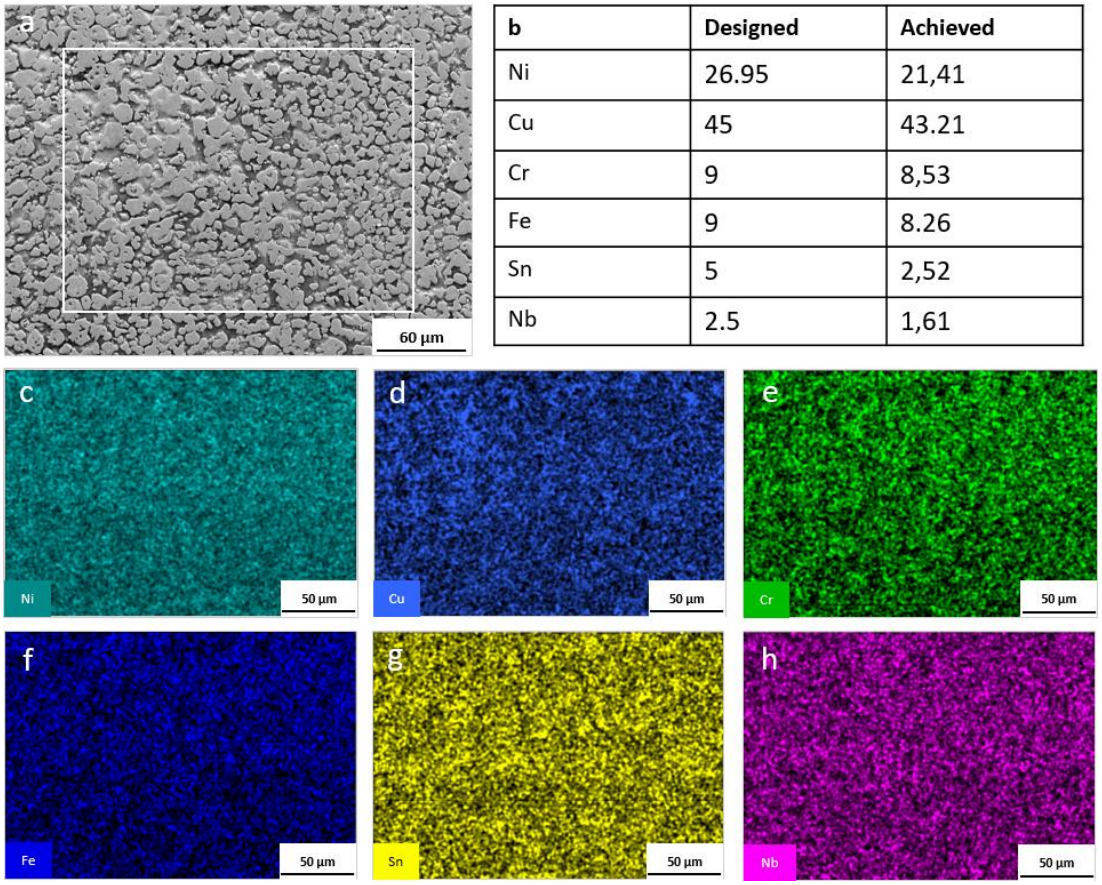

Figure 27 EDS mapping results: (a) SEM image of the investigated area, (b) achieved and desired elemental compositions in weight percent, (c-h) EDS mapping for Ni, Cu, Cr, Fe, Sn, Nb

Thermochemical modeling for In718-CuSn10 50% - 50% FGM structure requires deposited structure composition. Even though EDS mapping results in Fig 27. can provide the weight percentages of the components which present large amounts, this experimental method cannot determine the weight percentages of the components in small amounts. Thus, to solve this problem, the main powder composition (Table 1) is used. After related calculations, the thermochemical modelling executed as 26.95% Ni, 45% Cu, 9 % Cr, 9% Fe, 5% Sn, 2.5% Nb, 1.5% Mo, 0.5% Ti.

Additionally, X-ray fluorescence analysis of FGM structure has been conducted by using Niton XL3t GOLDD+ XRF Analyzer (Thermo Scientific) equipment to determine the chemical composition of the end product. According to the XRF analysis, FGM chemical composition is 25.68% Ni, 45.25% Cu, 9.97% Cr, 8.97% Fe, 5.16% Sn, 2.74% Nb, 1.56% Mo, 0.532% Ti. It has been seen that the results were very similar to the designed composition.

Thermochemical calculation results can be seen in Fig. 28, which represents the phase changes of the alloy under non-equilibrium condition and within a temperature range from 200 °C to 1700 °C. The single liquid melt is first separated into two immiscible liquid phases with different compositions at ~ 1550 °C. According to the calculation, the formation of the Cu-Ni rich first phase particles at ~ 1200 °C (fcc#1 Cu-Ni-Cr-Fe-Sn-Nb-Mo-Ti-Al system) are followed by the formation of Ni-Nb rich second phase particles (fcc#2 Ni-Nb-Cr-Fe-Cu-Ti-Sn-Mo-Al) at ~ 1050° C. The solidification of both copper-rich and nickel-rich alloys is complete at ~ 950 °C and 750 °C, respectively. A Cu-Sn rich bcc phase formation is observed just before the end of the last liquid phase at ~950° C. Before the liquid phase is depleted, the other possible phases such as Ni3Ti and Ni3Sn2 expected to form.

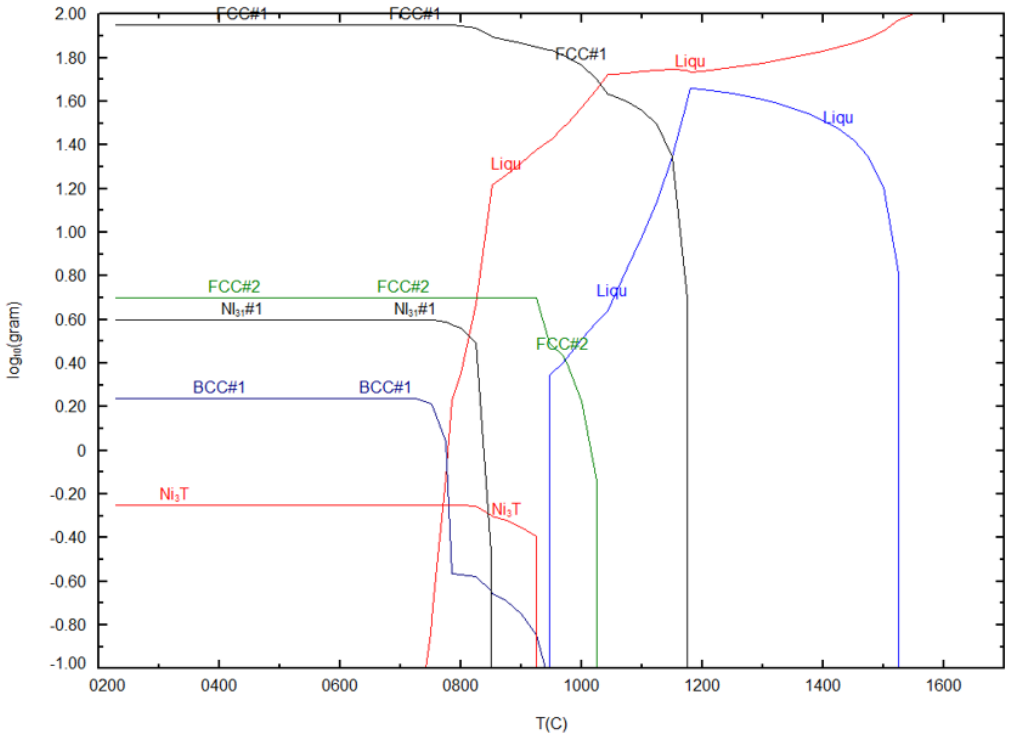

Figure 28 Non-equilibrum cooling calculation of 50:50 mixture (by weight) of CuSn10:Inconel718 alloy using FactSage™.

Additionally, EDS line analysis was conducted to be able to understand the participation behavior and evaluate the thermochemical analysis through these findings. Fig 29. shows back scattered electron detector image from random location of the structure with the paths adjusted for EDS line analysis. As EDS mapping shows, Ni, Cu, Sn, Nb and Cr have high amounts. Thermochemical modelling results predicts two different fcc phase, one of them was fcc#1 which is rich in Cu, Ni and Cr and the other one was fcc#2 which is rich in Ni and Nb. There is a big resemblance between fcc#1 and EDS line analysis results for location 1 and location 4 which are also rich in Ni, Cu and Cr and can be seen from Fig 30. Another phase that has been predicted by nonequilibrium calculation was bcc#1 which is rich in Cu and Sn. EDS line analysis results for location 3 shows similar weight percentages with bcc#1 thermochemical prediction.

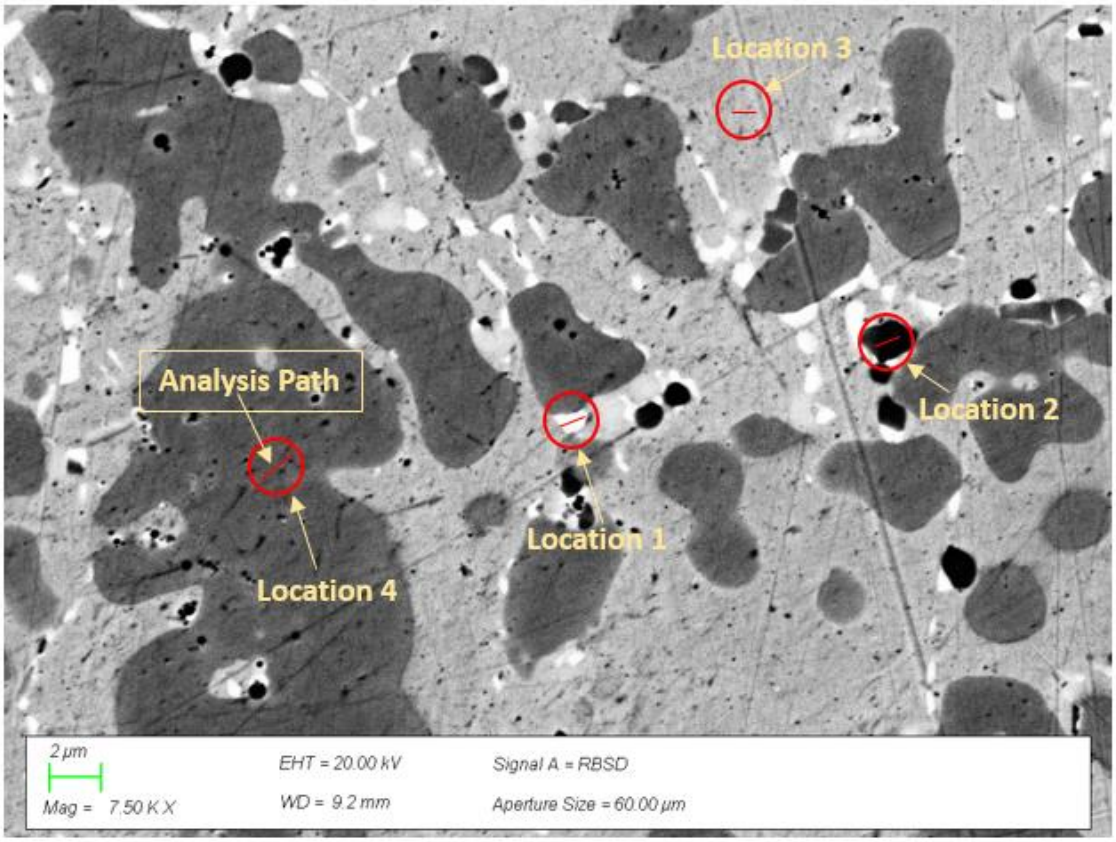

Figure 29 Back scattered electron detector image of Inconel 718 – CuSn10 gradient structures with the paths adjusted for elemental analysis by energy dispersive spectroscopy

EDS Line Analysis From Location 1

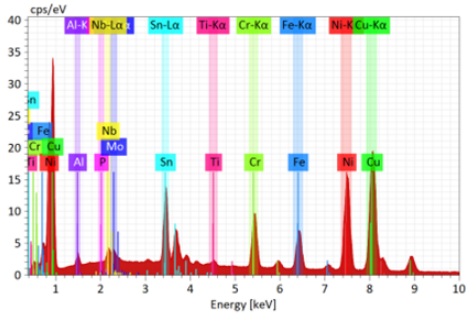

Element	Weight [%]	Atom [%]
Cu	43.68	47.87
Sn	5.34	6.02
Ni	25.56	30.33
Fe	6.53	8.15
Cr	6.48	8.68
Nb	0.26	0.19
Al	0.27	0.68
Ti	0.66	0.95

Possible Phase: FCC#1

EDS Line Analysis From Location 2

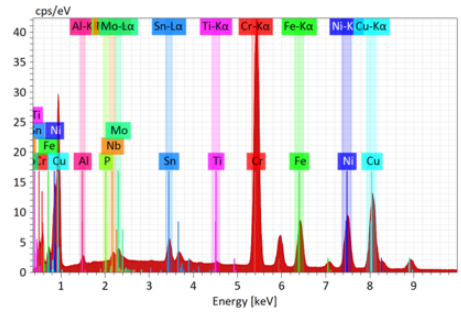

Element	Weight [%]	Atom [%]
Cu	30.49	29.17
Sn	2.34	1.20
Ni	16.78	17.39
Fe	9.80	10.67
Cr	34.38	40.20
Nb	0.26	0.17
Al	0.21	0.48
Ti	0.31	0.39

Possible Phase: BCC#2 from equilibrium modelling

EDS Line Analysis From Location 3

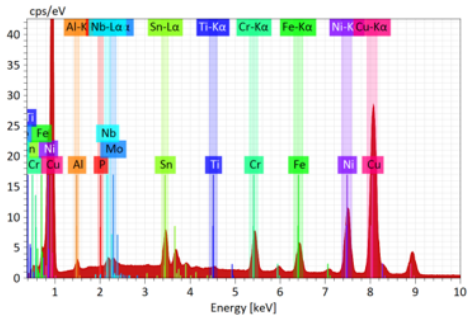

Element	Weight [%]	Atom [%]
Cu	60.72	63.74
Sn	3.83	4.11
Ni	17.65	20.06
Fe	5.01	5.98
Cr	4.98	5.35
Nb	0.13	0.09
Al	0.27	0.29
Ti	0.66	0.92

Possible Phase: BCC#1

EDS Line Analysis From Location 4

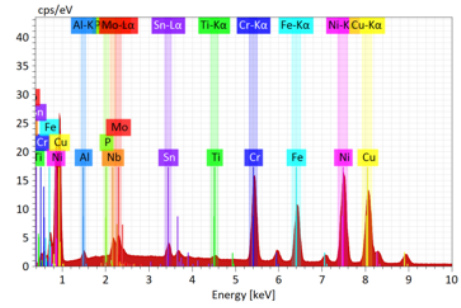

Element	Weight [%]	Atom [%]
Cu	32.15	32.53
Sn	1.77	0.96
Ni	30.88	33.83
Fe	12.25	14.10
Cr	12.40	15.33
Nb	1.48	1.02
Al	0.25	0.59
Ti	0.49	0.52

Possible Phase: FCC#1

Figure 30 The EDS analysis results of the locations shown in Fig 29. And possible phases

Another finding from our EDS line analysis is that formation of Cr rich phase. However, there was no indication about the Cr rich phase formation on the nonequilibrium calculation predictions. Related studies state that elemental distribution of those elements such as Cr, Si and C is rather hard to predict with Scheil solidification model [89]. Segregation behavior for Cr seems to be underestimated in Scheil. Similarly, these inconsistency problems between predicted equilibrium phases and experimental data have been discussed in various studies [61, 35, 101]. It is stated that thermochemical calculation predictions and experimental results may not always match. The reason behind this problem is that CALPHAD calculation does not cover the identical thermal history of the manufacturing process. Although it should be noted that Cr rich phase was predicted in the equilibrium conditioned thermochemical modelling as bcc#1.

Fcc#2 phase predicted by non-equilibrium cooling calculations shows similar elemental weight percentage and content as Location 5 which can be seen in Fig. 31.

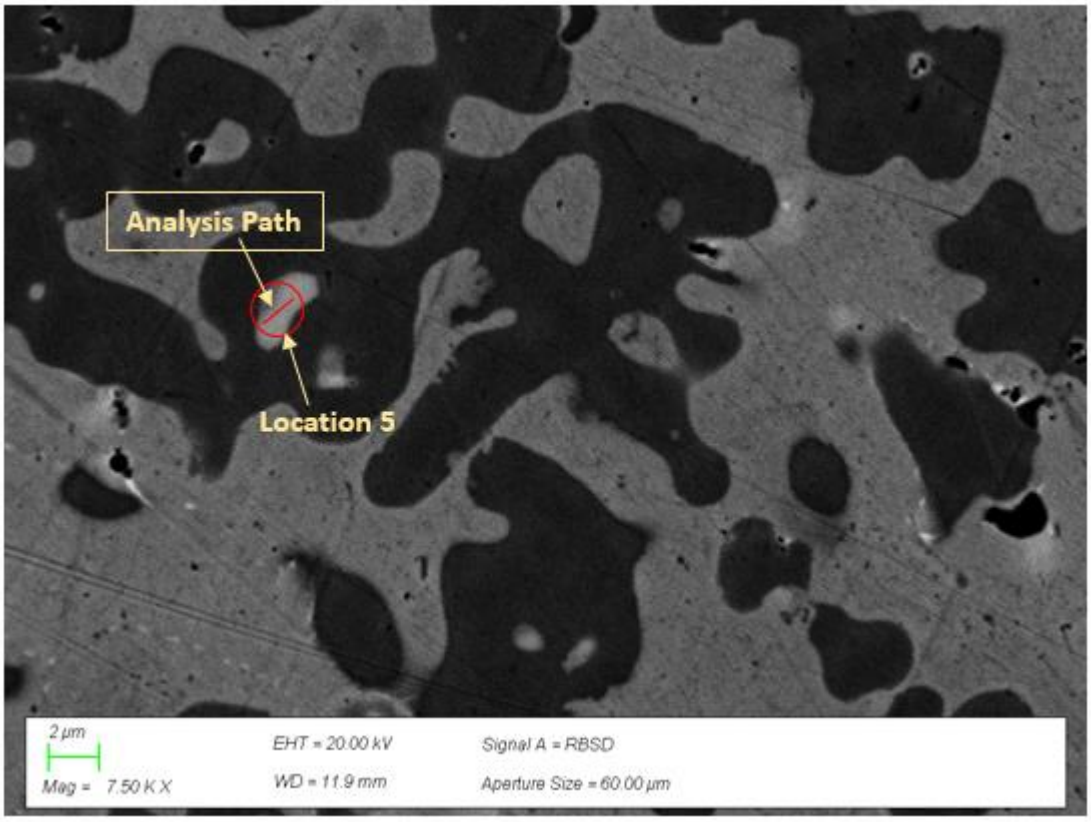

Figure 31 Back scattered electron detector image of Inconel 718 – CuSn10 gradient structures with the paths adjusted for elemental analysis by energy dispersive spectroscopy Nb Rich Location

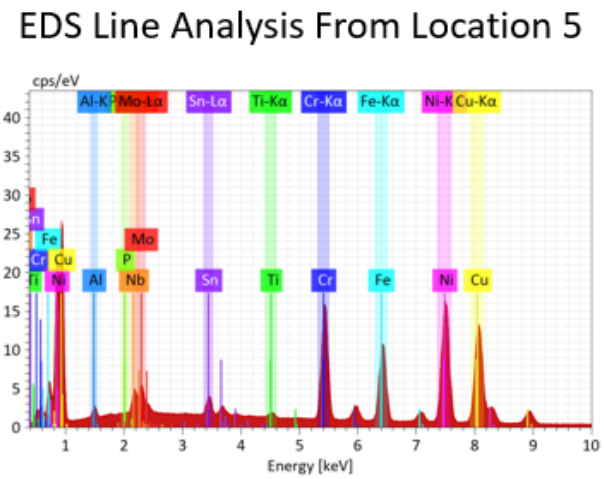

Element	Weight [%]	Atom [%]
Cu	30.71	32.76
Sn	2.49	1.42
Ni	25.12	29.01
Fe	9.72	11.80
Cr	10.30	13.43
Nb	9.03	6.59
Al	0.21	0.53
Ti	0.81	1.14

Possible Phase: FCC#2

Figure 32 The EDS analysis results of the location 5 shown in Fig 31. And possible phases

Throughout the experimental study, it has been seen that CuSn10 does require more total energy input than In718, even though CuSn10 have lower melting point. This can be explained by the high reflectivity property of copper.

The XRD results obtained from a random location in gradient structure confirms the phase predictions of the Scheil solidification models as well as the results of EDS analysis. As can be seen from Fig. 33, Ni-Cu rich fcc1 phase, Cu-Sn rich bcc1 and Ni3Sn2 phase obtained from the XRD patterns matches with the solidification model. According to these results it is safe to say that fully integrated solid solution of 50%-50% Inconel 718 – CuSn10 FGM is obtained since we can verify the four phases that were predicted in the Scheil and EDS analyses with the XRD results. In the post processing of the XRD results, single element Cr peak was obtained in the same region where Ni-Cu observed. Cr rich phase was also predicted in the equilibrium condition calculation. The validation of the Scheil shows that, both In718-CuSn10 fcc structure helped to obtain an integrated structure.

Overall, the designed and the predicted crystallographic, elemental, geometrical properties validated through microstructural investigations.

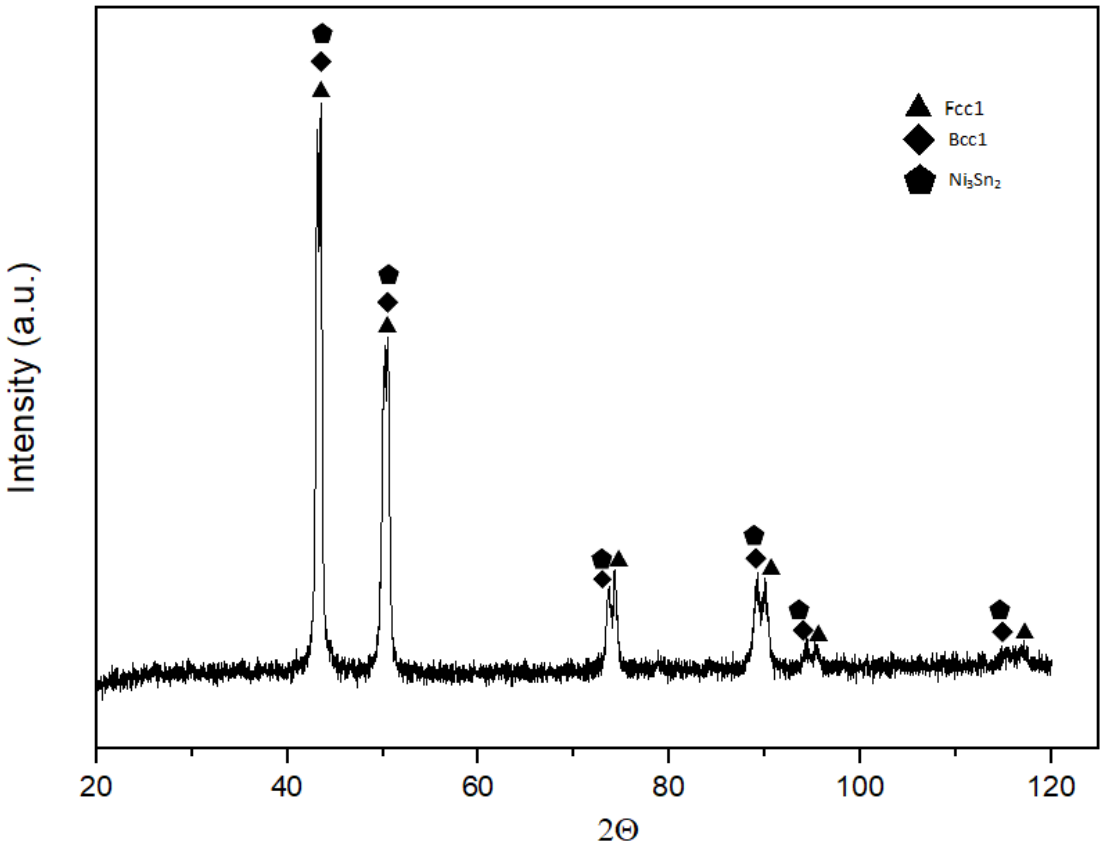

Figure 33 X-Ray diffraction results of In718-CuSn10 FGM structure

To compare the mechanical properties, microhardness measurements were taken by utilizing INNOVATEST Falcon 500. The used parameters were, 200g as load and 15s as dwell time. Each specimen was polished before the measurements.

Figure 34 INNOVATEST Falcon 500 Microhardness Tester [102]

Fig 35. represents microhardness profiles of 50%-50% In718-CuSn10 FGM, In718, and CuSn10 structures. Measurements start from the 4 mm higher than the base surface and continues along building directions with 2 mm intervals.

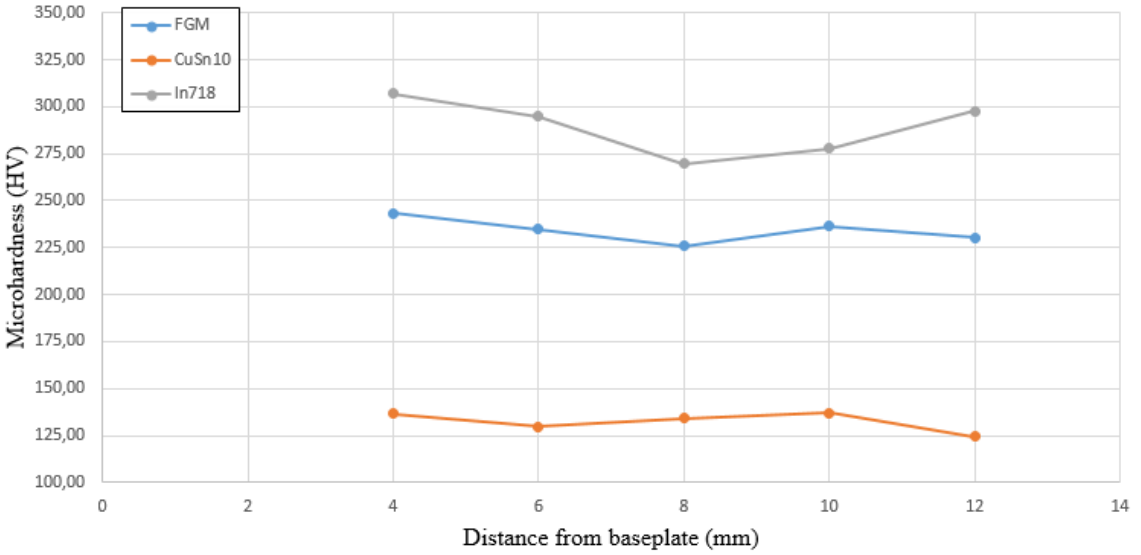

Figure 35 Microhardness profiles of 50%-50% In718-CuSn10 FGM (blue line), In718 (grey line), CuSn10 (orange line) structures

The microhardness results were obtained from five indentation points for each structure. For In 718, microhardness values changed between 306,97 ± 6,1 HV and 269,52 ± 3 HV throughout 8 mm path, where CuSn10 microhardness values changed between 137,01 ± 2,9 HV and 124,26 ± 4,8 HV. Smooth transition can be validated through FGM microhardness results. The microhardness values for the FGM structure were changed between 243,44 ± 13,4 HV and 225,76 ± 12,4 HV.

It can be seen that the FGM structure's hardness profile is similar to the In718 hardness profile at the beginning. But as the height increases, the similarity of hardness profile changes towards CuSn10. Also, a slight decrease in microhardness results was seen as the distance from the bottom surface increased, the same behavior was reported in the literature for titanium alloys which were fabricated with DED [103]. The microhardness values for fabricated In718 and CuSn10 structures were found to be higher 36,93 HV and 2,34 HV respectively than wrought In718 and CuSn10 structures.

The microhardness value for FGM structure is 101,83 HV higher than the CuSn10 microhardness value. Thus, we can say that better mechanical properties than CuSn10 but slightly decreased mechanical properties than In 718, successfully obtained with the 50%-50% In718-CuSn10 FGM structure.

To evaluate and compare thermophysical properties between In718, CuSn10, and FGM structure, thermal diffusivity, specific heat capacity, and density measurements were conducted for each material. And then thermal conductivity values calculated for each material.

The thermal diffusivity measurements were taken by utilizing the NETZSCH LFA 457 MicroFlash® which can be seen in Fig. 36. The fabricated 50%-50% In718-CuSn10 FGM, In718, and CuSn10 structures were tested according to the ASTM E1461 standard method for thermal diffusivity by the flash method. The test was executed within the temperature range of 25°C-350°C with 50°C increments, for each temperature point three measurements were taken.

Figure 36 NETZSCH LFA 457 MicroFlash®[104]

Thermal diffusivity results for each material can be seen in Fig. 37. as a function of the temperature. The thermal diffusivity measurements for In718 were between 2,87 ± 0,04 mm^2/s and 3,88 ± 0,06 mm^2/s for 25° to 350°C, respectively. These results are very similar to the thermal diffusivity values of In718 which are reported in literature [17]. For CuSn10, thermal diffusivity values were between 19,47 ± 0,44 mm^2/s and 25,88 ± 0,06 mm^2/s for 25°C to 350°C, respectively. Similar values were also reported in the literature for CuSn10 [105]. Thermal diffusivity values for 50%-50% In718-CuSn10 FGM structure ranged between 8,13 ± 0,17 mm^2/s and 10,61 ± 0,03 mm^2/s for 25°C to 350°C, respectively. Thermal diffusivity of FGM structure nearly tripled the thermal diffusivity value of In 718. The thermal diffusivity measurements show that enhanced thermophysical properties were achieved with the FGM structure compared to the In718 structure. But to be able to evaluate and fully understand the thermophysical properties for each material, a thermal conductivity calculation was conducted. Prior to the calculation of thermal conductivity, specific heat and density tests were conducted.

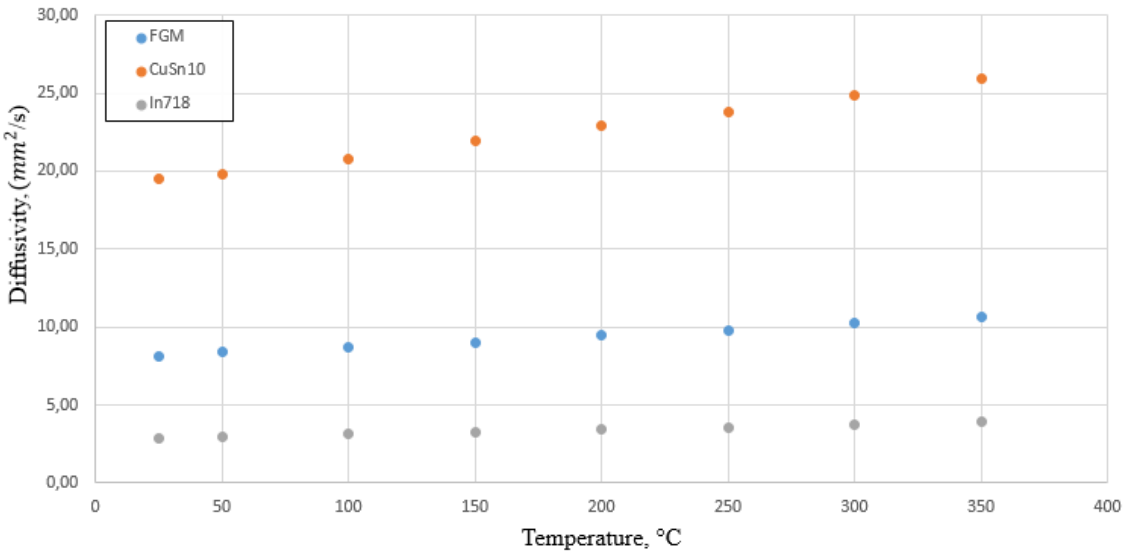

Figure 37 Thermal diffusivity measurements for In718, CuSn10 and FGM structures

The densities of fabricated CuSn10, In718, and FGM structures were calculated by using the Archimedes method. Density values calculated as 8,6150 g/cc, 8,1853 g/cc and

8,4840 g/cc for CuSn10, In718 and FGM structure respectively. These values were used in thermal conductivity calculations.

The specific heat capacity (c_p) measurements were taken by utilizing the NETZSCH STA 449 F3 Jupiter® which can be seen in Fig. 38. The fabricated 50%-50% In718-CuSn10 FGM, In718, and CuSn10 structures were tested according to the ASTM E1269 standard test method for determining specific heat capacity by differential scanning calorimetry. The test was executed within the temperature range of 25°C-350°C with 50°C increments.

Figure 38 NETZSCH STA 449 F3 Jupiter® [106]

The specific heat capacity (c_p) results for each material as a function of temperature can be seen in Fig. 39. The specific heat capacity values for In718 were between 0,3252 and 0,3902 ($J/(g * °K)$) for 25° to 350°C, respectively. These results are very similar to the specific heat capacity values of In718 which are reported in literature [17]. For CuSn10, the specific heat capacity values were between 0,3388 and 0,4363 ($J/(g * °K)$) for 25°C to 350°C, respectively. Similar values were also reported in the literature for CuSn10 [105]. The specific heat capacity values for 50%-50% In718-CuSn10 FGM structure ranged between 0,4020 and 0,4995 ($J/(g * °K)$) for 25°C to 350°C, respectively. As can

be seen from the results, the specific heat capacity values of the FGM structure are higher than In718 and CuSn10 ones. This is a result of combining two different materials and enriching the chemical composition of the structure since the specific heat capacity is affected by the chemical composition. Nevertheless, the specific heat capacity values do not affect the thermal conductivity as much as thermal diffusivity.

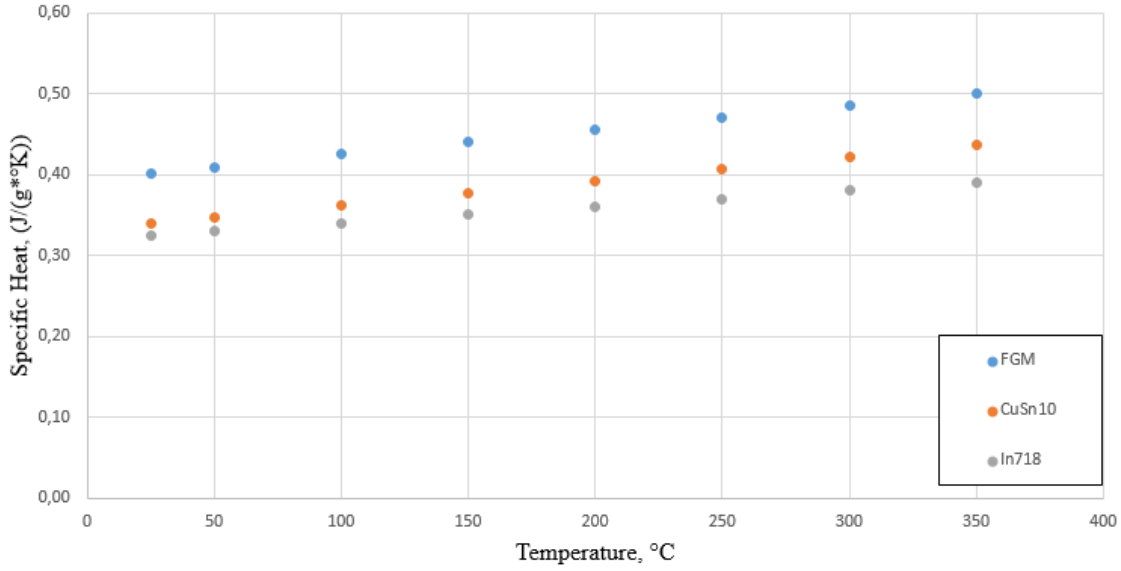

Figure 39 Specific heat capacity measurements for In718, CuSn10 and FGM structures

Thermal conductivity values for In718, CuSn10, and 50%-50% In718-CuSn10 FGM structures were calculated by using the relationship between specific heat capacity (c_p), thermal diffusivity (α), thermal conductivity (λ), and density (ρ), which can be seen in Equation 4.1.

$$\alpha = \frac{\lambda}{c_p * \rho} \tag{4.1}$$

The calculated thermal conductivity values for each material can be seen in Fig. 40. as a function of temperature. The thermal conductivity values for In718 were between 7,66 $(W/m.K)$ and 12,40 $(W/m.K)$ for 25° to 350°C, respectively. These results are very similar to the thermal conductivity values of In718 which are reported in the literature [17]. For CuSn10, thermal conductivity values were between 56,84 $(W/m.K)$ and 97,29

(W/m. K) for 25°C to 350°C, respectively. Similar values were also reported in the literature for CuSn10 [105]. The thermal conductivity values for 50%-50% In718-CuSn10 FGM structure ranged between 27,73 (W/m. K) and 44,99 (W/m. K) for 25°C to 350°C, respectively.

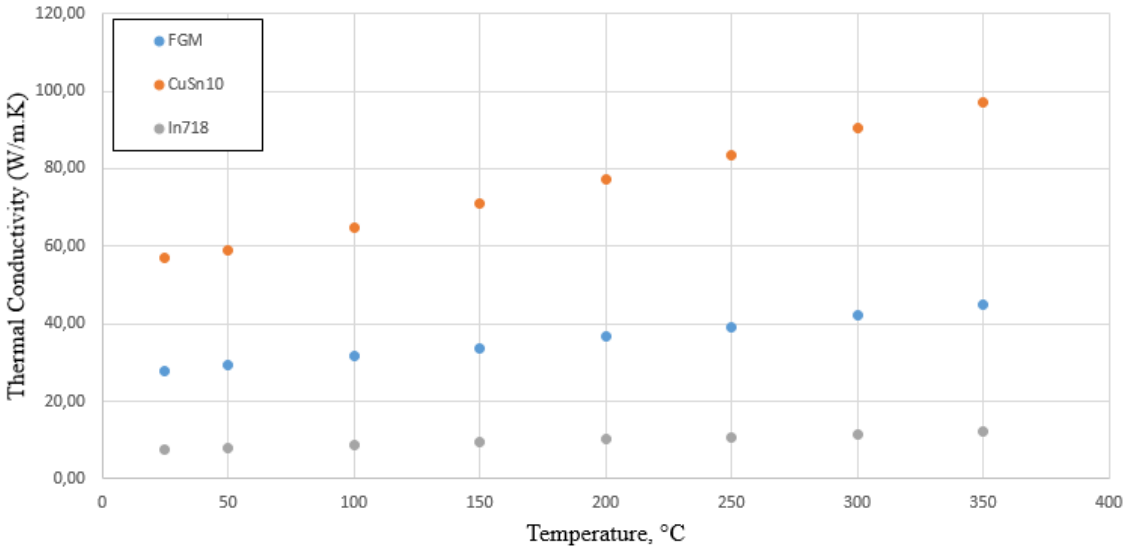

Figure 40 Thermal conductivity values for In718, CuSn10 and FGM structures

The results show that, approximately %360 increase in thermal conductivity and approximately %270 increase in thermal diffusivity obtained in the FGM structure with respect to the In718 structure. The trends of thermal conductivity and thermal diffusivity were similar to each other within the temperature range of 25°C to 350°C.

With these results, we can validate that it is possible to obtain better thermophysical properties than In718 alloy and higher mechanical properties than CuSn10 alloy by combining these two materials as FGM structures.

5. CONCLUSION

This thesis covers directed energy deposition process parameter development, microstructural investigations and evaluation, thermochemical modeling for 50%-50% CuSn10-In718 FGM structure. First, single material optimizations were conducted experimentally by changing total energy input values and validating optimized structures according to their porosity levels, dilution, bonding behaviors and geometrical shapes. After that, process parameter optimization was conducted for FGM structures by starting with single track trials. The optimized single material parameters helped to understand the behavior of FGM structure, and these parameters were used to get initial trials. The evaluation of optimized process parameter and successful deposition for FGM structure has been done by investigating the microstructure and elemental composition with scanning electron microscopy (SEM), back scattered electron detector (BSE), x-ray diffractometer (XRD) and energy dispersive spectroscopy (EDS). Additionally, thermochemical modelling was conducted for %50-%50 CuSn10-In718 FGM structure to demonstrate that the phase equilibrium is predicted for such system. Non-equilibrium Schel solidification was utilized for the thermochemical modelling since DED process has rapid cooling. The evaluation and validation between thermochemical modelling results and microstructural results has been conducted.

Overall, functionally graded Inconel 718 – CuSn10 structure have been successfully fabricated by using directed energy deposition. Single track trials gave an insight for initial process parameters since we can understand the bonding behavior of the related material by fabricating such structures. The microstructural examinations of graded structures show no indication of distinct structural, compositional or microstructural boundaries. A fine dendritic structure aligned along building direction was observed without any delamination. By using CALPHAD method, thermodynamic calculations

have been conducted to predict and evaluate the stable phases within 50%-50% Inconel 718-CuSn10 gradient structure while EDS mapping shows evenly distributed elemental composition throughout the structure. The validation of the predicted phases from Scheil computation has been achieved through SEM, EDS area mapping, EDS line analysis and X-Ray diffraction. Also, it has been found that Scheil modelling phase prediction is more efficient than the equilibrium modelling since the most of the validated phases through microstructural investigation were predicted by Scheil modelling. This study shows the feasibility of fabricating gradient nickel-copper alloy using directed energy deposition. Also, it has been demonstrated that CALPHAD based thermodynamic computation is viable method for designing the gradient structures. Furthermore, microhardness and thermal conductivity tests has been conducted to compare the mechanical and thermophysical properties between 50%-50% CuSn10-In718, In718, and CuSn10 structures. According to the results, it has been shown that it is possible to improve thermophysical properties and mechanical properties of the original alloys by fabricating a In718-CuSn10 FGM structure with directed energy deposition process. It is foreseeable that by using the developed methodologies, next-generation aerospace & nuclear parts with better mechanical and thermal properties can be designed and manufactured.

References

1. A. Mortensen, S. Suresh, Functionally graded metals and metal-ceramic composites: part 1 Processing, Int. Mat. Rev. 40 (6) (1995) 239-265.
2. Gururaja Udupal, S.Shrikantha rao, K.V.Gangadharan, International Conference on Advances in Engineering, Science and Management 2012.
3. S. Suresh, A. Mortensen, Fundamentals of Functionally Graded Materials, IOM Communications Ltd, London, 1998.
4. M. Shakil, M. Ahmad, N.H. Tariq, B.A. Hasan, J.I. Akhter, E. Ahmed, M. Mehmood, M.A. Choudhry, M. Iqbal, Microstructure and hardness studies of electron beam welded inconel 625 and stainless steel 304L, Vacuum 110 (2014) 121-126.
5. V. Birman, L.W. Byrd, Modeling and analysis of functionally graded materials and structures, Appl. Mech. Rev. 60 (5) (2007) 195.
6. Z. Sun, J.C. Ion, Review laser welding of dissimilar metal combinations, J. Mat. Sci. 30 (1995) 4025-4214.
7. F. Findik, Recent developments in explosive welding, Mat. Des. 32 (3) (2011) 1081-1093.
8. R.W. Messler, Principles of Welding: Processes, Physics, Chemistry, and Metallurgy, John Wiley & Sons, Inc., New York, 1999.
9. A. Bandyopadhyay, B. Heer, Additive manufacturing of multi-material structures, Mater. Sci. Eng. R Rep. 129 (2018) 1–16.
10. M. Fazel-Najafabadi, S.F. Kashani-Bozorg, A. Zarei-Hanzaki, Joining of CP-Ti to 304 stainless steel using friction stir welding technique, Mater. Des. 31 (10) (2010) 4800–4807.
11. Z. Sun, R. Karrpi, The application of electron beam welding for the joining of dissimilar metals: an overview, J. Mater. Process. Technol. 59 (1996) 257–267.
12. H.C. Chen, A.J. Pinkerton, L. Li, Fibre laser welding of dissimilar alloys of Ti-6Al-4V and Inconel 718 for aerospace applications, Int. J. Adv. Manuf. Technol. 52 (2010) 977–987.
13. S.A. David, T. Debroy, Current issues and problems in welding science, Science 257 (5069) (1992) 497–502.

14. Kieback B, Neubrand A, Riedel H. Processing techniques for functionally graded materials. Mater Sci Eng, A 2003;362(1-2):81-106.
15. J.J. Sobczak, L. Drenchev, Metallic functionally graded materials: a specific class of advanced composites, J. Mater. Sci.Technol. 29 (4) (2013) 297-316
16. R.M. Mahamood, E.T. Akinlabi, Functionally Graded Materials, Springer International Publishing, AG Switzerland, 2017.
17. ATI METALS, Alloy 718, Technical Datasheet, NI105 Version 2, February, 2011.
18. D.L. Ellis, GRCop-84: A High-Temperature Copper Alloy for High-Heat-Flux Applications, (2005) NASA Report NASA/TM—2005-213566.
19. H.C. de Groh III, D.L. Ellis, W.S. Loewenthal, Comparison of GRCop-84 to other Cu alloys with high thermal conductivities, J. Mater. Eng. Perform. (2007) 1–24.
20. K. Chen, C. Wang, Q. Hong, S. Wen, Y. Zhou, C. Yan, Y. Shi, Selective laser melting 316L/CuSn10 multi-materials: Processing optimization, interfacial characterization and mechanical property Journal of Materials Processing Tech. 283 (2020) 116701.
21. B. Heer, A. Bandyopadhyay, Compositionally graded magnetic-nonmagnetic bimetallic structure using laser engineered net shaping, Mater. Lett. 216 (2018) 16.
22. X. Mei, X. Wang, Y. Peng, H. Gu, G. Zhong, S. Yang, Interfacial characterization and mechanical properties of 316L stainless steel/inconel 718 manufactured by selective laser melting, Mater. Sci. Eng., A 758 (2019) 185–191.
23. S.L. Sing, W.Y. Yeong, Laser powder bed fusion for metal additive manufacturing: perspectives on recent developments, Virtual Phys. Prototyping 15 (3) (2020) 359–370.
24. W.E. Frazier, Metal additive manufacturing: a review, J. Mat. Eng. Perform. 23 (6) (2014) 1917-1928.
25. R. Banerjee, P.C. Collins, D. Bhattacharyya, S. Banerjee, H.L. Fraser, Microstructural evolution in laser deposited compositionally graded alpha/beta titaniumevanadium alloys, Acta Mat. 51 (11) (2003) 3277-3292.

26. P.C. Collins, R. Banerjee, S. Banerjee, H.L. Fraser, Laser deposition of compositionally graded titaniumevanadium and titaniumemolybdenum alloys, Mat. Sci. Eng. A 352 (1-2) (Jul. 2003) 118-128.
27. H. Fayazfar, M. Salarian, A. Rogalsky, D. Sarker, P. Russo, V. Paserin, E. Toyserkani, A critical review of powder-based additive manufacturing of ferrous alloys: Process parameters, microstructure and mechanical properties, Materials & Design 144 (2018) 98–128.
28. D.C. Hofmann, K.S. Vecchio, Submerged friction stir processing (SFSP): an improved method for creating ultra-fine-grained bulk materials, Mat. Sci. Eng. A 402 (1-2) (Aug. 2005) 234-241.
29. T. Qian, D. Liu, X. Tian, C. Liu, H. Wang, Microstructure of TA2/TA15 graded structural material by laser additive manufacturing process, Trans. Nonferrous Met. Soc. China 24 (9) (2014) 2729-2736.
30. H.S. Ren, D. Liu, H.B. Tang, X.J. Tian, Y.Y. Zhu, H.M. Wang, Microstructure and mechanical properties of a graded structural material, Mat. Sci. Eng. A 611 (2014) 362-369
31. D.C. Hofmann, S. Roberts, R. Otis, J. Kolodziejska, R.P. Dillon, J.-O. Suh, A. a Shapiro, Z.-K. Liu, J.-P. Borgonia, Developing gradient metal alloys through radial deposition additive manufacturing, Sci. Rep. 4 (2014) 5357.
32. D.T Sarathchandra, S. Kanmani Subbu, N. Venkaiah, Functionally graded materials and processing techniques: An art of review, Materials Today: Proceedings 5 (2018) 21328-21334.
33. S. Dhomne, A.M. Mahalle, Thermal barrier coating materials for SI engine, Journal of Materials Research and Technology (2018)
34. U. Savitha, et al., Additive Laser Deposition of YSZ on Ni Base Superalloy for Thermal Barrier Application, Surface and Coatings Technology, 2018
35. L.D. Bobbio, B. Bocklund, R. Otis, J.P. Borgonia, R.P. Dillon, A.A. Shapiro, B. McEnerney, Z. Liu, A.M. Beese, Characterization of a functionally graded material of Ti-6Al-4V to 304L stainless steel with an intermediate V section, J. Alloys Compd. 742 (2018) 1031-1036, https://doi.org/10.1016/ j.jallcom.2018.01.156.
36. M.M. Nemat-Alla, M.H. Ata, M.R. Bayoumi, W. Khair-Eldeen, Powder metallurgical fabrication and microstructural investigations of aluminum/steel functionally graded material, Mater. Sci. Appl. 2 (12) (2011) 1708.

37. P. Samal, J. Newkirk, Powder Metallurgy Methods and Applications vol. 7, ASM Handbook of Powder Metallurgy, 2015.
38. Gibson, I., Rosen, D., Stucker, B., 2015. Additive Manufacturing Technologies: 3D Printing, Rapid Prototyping, and Direct Digital Manufacturing, Springer-Verlag, New York. https://doi.org/10.1007/978-1-4939-2113-3.
39. M. Zhou, J. Xi, J. Yan, Modeling and processing of functionally graded materials for rapid prototyping, J. Mater. Process. Technol. 146 (3) (2004) 396–402.
40. J. Huang, G.M. Fadel, V.Y. Blouin, M. Grujicic, Bi-objective optimization design of functionally gradient materials, Mater. Des. 23 (7) (2002) 657–666.
41. A. Pasko, V. Adzhiev, A. Sourin, V. Savchenko, Function representation in geometric modeling: concepts, implementation and applications, Vis. Comput. 11 (8) (1995) 429–446.
42. W. Chiu, S. Tan, Multiple material objects: from CAD representation to data format for rapid prototyping, Comput. Aided Des. 32 (12) (2000) 707–717.
43. A.C.F.o.A.M. Technologies, A.C.F.o.A.M.T.S.F.o Terminology, Standard Terminology for Additive Manufacturing Technologies, ASTM International, 2012.
44. Zhang, Y., Jarosinski, W., Jung, Y.-G., Zhang, J., 2018c. Additive manufacturing processes and equipment. Additive Manufacturing. Elsevier, pp. 39–51. https://doi. org/10.1016/B978-0-12-812155-9.00002-5.
45. Additive manufacturing, https://www.manufacturingguide.com/en/additiv-tillverkning, (2013).
46. Reichardt A, et al. Advances in additive manufacturing of metal-based functionally graded materials. Int Mater Rev 2020:1-29
47. T.D. Ngo, A. Kashani, G. Imbalzano, K.T. Nguyen, D. Hui, Additive manufacturing (3D printing): a review of materials, methods, applications and challenges, Compos. B Eng. 143 (2018) 172–196.
48. J.-Y. Lee, J. An, C.K. Chua, Fundamentals and applications of 3D printing for novel materials, Appl. Mater. Today 7 (2017) 120–133.
49. Demir AG, Previtali B. Multi-material selective laser melting of Fe/Al-12Si components. Manufacturing letters 2017;11:8-11.
50. Han C, et al. Titanium/hydroxyapatite (Ti/HA) gradient materials with quasi-continuous ratios fabricated by SLM: Material interface and fracture toughness. Mater Des 2018;141:256-66.

51. Tan C, Zhou K, Kuang T. Selective laser melting of tungsten-copper functionally graded material. Mater Lett 2019;237:328-31.
52. Li Y, et al. Additively manufactured functionally graded biodegradable porous iron. Acta Biomater 2019;96:646-61.
53. Popovich V, et al. Functionally graded Inconel 718 processed by additive manufacturing: crystallographic texture, anisotropy of microstructure and mechanical properties. Mater Des 2017;114:441-9.
54. Al-Saedi DS, et al. Mechanical properties and energy absorption capability of functionally graded F2BCC lattice fabricated by SLM. Mater Des 2018;144:32-44.
55. Bhavar V, et al. A review on functionally gradient materials (FGMs) and their applications. In: IOP conference series: materials science and engineering. IOP Publishing; 2017.
56. Reza Ghanavati et al. Additive manufacturing of functionally graded metallic materials: A review of experimental and numerical studies (2021).
57. Yan L, Chen Y, Liou F. Additive manufacturing of functionally graded metallic materials using laser metal deposition. Additive Manufacturing 2020;31:100901
58. Hofmann, D.C., Kolodziejska, J., Roberts, S., Otis, R., Dillon, R.P., Suh, J.-O., Liu, Z.-K., Borgonia, J.-P., 2014. Compositionally graded metals: a new frontier of additive manufacturing. J. Mater. Res. 29, 1899–1910. https://doi.org/10.1557/ jmr.2014.208.
59. Mukherjee, T., Zuback, J.S., De, A., DebRoy, T., 2016. Printability of alloys for additive manufacturing. Sci. Rep. 6, 19717 https://doi.org/10.1038/srep19717.
60. DebRoy, T., Wei, H.L., Zuback, J.S., Mukherjee, T., Elmer, J.W., Milewski, J.O., Beese, A. M., Wilson-Heid, A., De, A., Zhang, W., 2018. Additive manufacturing of metallic components – process, structure and properties. Prog. Mater. Sci. 92, 112–224. https://doi.org/10.1016/j.pmatsci.2017.10.001.
61. L.D. Bobbio, R.A. Otis, J.P. Borgonia, R.P. Dillon, A.A. Shapiro, Z. Liu, A.M. Beese, Additive manufacturing of a functionally graded material from Ti-6Al-4V to Invar: experimental characterization and thermodynamic calculations, Acta Mater. 127 (2017) 133-142, https://doi.org/10.1016/j.actamat.2016.12.070.
62. Sahasrabudhe, H., Harrison, R., Carpenter, C., Bandyopadhyay, A., 2015. Stainless steel to titanium bimetallic structure using LENSTM. Addit. Manuf. 5, 1–8. https://doi. org/10.1016/j.addma.2014.10.002.

63. Beal, V.E., Erasenthiran, P., Hopkinson, N., Dickens, P., Ahrens, C.H., 2004. Fabrication of x-graded H13 and Cu powder mix using high power pulsed Nd:YAG laser. In: Proceedings of Solid Freeform Fabrication Symposium. Austin, Texas, pp. 187–197.

64. Noecker, F.F., DuPont, J.N., 2002. Functionally graded copper – steel using laser engineered net shapingTM process. In: International Congress on Applications of Lasers & Electro-Optics. Laser Institute of America, p. 185430. https://doi.org/ 10.2351/1.5066217.

65. Articek, U., Milfelner, M., Anzel, I., 2013. Synthesis of functionally graded material H13/ Cu by LENS technology. Adv. Prod. Eng. Manag. 8, 169–176. https://doi.org/ 10.14743/apem2013.3.164.

66. Onuike B. Additive manufacturing of Inconel 718—Copper alloy bimetallic structure using laser engineered net shaping (LENS™) (2018).

67. Saunders, N., Guo, U.K.Z., Li, X., Miodownik, A.P., Schill´e, J.P., 2003. Using JMatPro to model materials properties and behavior. JOM 55, 60–65. https://doi.org/10.1007/ s11837-003-0013-2.

68. Yan, J., Battiato, I., Fadel, G.M., 2018. Planning the process parameters for the direct metal deposition of functionally graded parts based on mathematical models. J. Manuf. Process. 31, 56–71. https://doi.org/10.1016/j.jmapro.2017.11.001.

69. Muller, P., Mognol, P., Hascoet, J.-Y., 2013. Modeling and control of a direct laser powder deposition process for functionally graded Materials (FGM) parts manufacturing. J. Mater. Process. Technol. 213, 685–692. https://doi.org/10.1016/ j.jmatprotec.2012.11.020.

70. Muller, P., Hascoet, J.-Y., Mognol, P., 2014. Toolpaths for additive manufacturing of functionally graded materials (FGM) parts. Rapid Prototyp. J. 20, 511–522. https:// doi.org/10.1108/RPJ-01-2013-0011.

71. B.E. Carroll, R.A. Otis, J.P. Borgonia, J. Suh, R.P. Dillon, A.A. Shapiro, D.C. Hofmann, Z. Liu, A.M. Beese, Functionally graded material of 304L stainless steel and Inconel 625 fabricated by directed energy deposition: characterization and thermodynamic modeling, Acta Mater. 108 (2016) 46-54, https://doi.org/10.1016/j.actamat.2016.02.019.

72. L.D. Bobbio, B. Bocklund, R. Otis, J.P. Borgonia, R.P. Dillon, A.A. Shapiro, B. McEnerney, Z. Liu, A.M. Beese, Experimental analysis and thermodynamic

calculations of an additively manufactured functionally graded material of V to Invar 36, J. Mater. Res. 33 (11) (2018) 1642-1649, https://doi.org/10.1557/jmr.2018.92.

73. N.K. Adomako, S. Noh, C. Oh, S. Yang, J.H. Kim, Laser deposition additive manufacturing of 17-4PH stainless steel on Ti-6Al-4V using V interlayer, Mater. Res. Lett. (2019) 259-266, https://doi.org/10.1080/21663831.2019.1596989.
74. W. Li, X. Chen, L. Yan, J. Zhang, X. Zhang, F. Liou, Additive manufacturing of a new Fe-Cr-Ni alloy with gradually changing compositions with elemental powder mixes and thermodynamic calculation, Int. J. Adv. Manuf. Technol. 95 (1) (2018) 1013-1023, https://doi.org/10.1007/s00170-017-1302-1.
75. DMG MORI LASERTEC 65 3D MONOBLOCK https://en.dmgmori.com/products/machines/additive-manufacturing/powder-nozzle/lasertec-65-ded-hybrid.
76. F.A. España, V.K. Balla, S. Bose, A. Bandyopadhyay, Design and fabrication of CoCrMo alloy based novel structures for load bearing implants using laser engineered net shaping, Mater. Sci. Eng. C 30 (2010) 50–57.
77. A. Simchi, H. Pohl, Effects of laser sintering processing parameters on the microstructure and densification of iron powder, Mater. Sci. Eng. A 359 (2003) 119–128.
78. H. Lee, C.H.J. Lim, M.J. Low, N. Tham, V.M. Murukeshan, Y.-J. Kim, Lasers in additive manufacturing: a review, Int. J. Precis. Eng. Manuf. Technol. 4 (2017) 307–322, https://doi.org/10.1007/s40684-017-0037-7.
79. C. Tan, K. Zhou, W. Ma, L. Min, Interfacial characteristic and mechanical performance of maraging steel-copper functional bimetal produced by selective laser melting based hybrid manufacture, Mater. Des. 155 (2018) 77–85, https://doi.org/10.1016/j.matdes.2018.05.064.
80. C. Zhao et al., Science 370 (6520) (2020) 1080–1086, https://doi.org/10.1126/science:abd1587.
81. ECLIPSE LV100ND (NIKON) www.nikonmetrology.com/en-gb/industrial-microscopes/upright-microscopes-eclipse-lv100nd .
82. Discotom 10 Struers https://www.struers.com/en/Products/Cutting/Cutting-equipment/Discotom#.

83. Ultra High Resolution FE-SEM for Versatile Analytics, SUPRA series, 2019 https://www.zeiss.com/microscopy/int/products/scanning-electron-microscopes.html.
84. L. Kaufman, J. Ågren, CALPHAD, first and second generation e Birth of the materials genome, Scr. Mat. 70 (Jan. 2014) 3-6.
85. L. Kaufman, H. Bernstein, Computer Calculation of Phase Diagrams, Academic Press, 1970.
86. C. W. Bale, E. Bélisle, P. Chartrand, S. A. Decterov, G. Eriksson, A.E. Gheribi, K. Hack, I. H. Jung, Y. B. Kang, J. Melançon, A. D. Pelton, S. Petersen, C. Robelin. J. Sangster, P. Spencer and M-A. Van Ende, FactSage Thermochemical Software and Databases - 2010 - 2016, Calphad, vol. 54, pp 35-53, 2016 www.factsage.com.
87. Z.-K. Liu, First-principles calculations and CALPHAD modeling of thermodynamics, J. Phase Equilibria Diffus. 30 (5) (Sep. 2009) 517-534.
88. Calphad presentation - Dr. C. Campbell, NIST https://thermocalc.com/content/uploads/Seminars_Presentations/calphad-and-beyond-the-true-story-of-materials-genome-ifam-2016.pdf.
89. Y. Liu, Y. Wang, X. Wu, J. Shi Nonequilibrium thermodynamic calculation and experimental investigation of an additively manufactured functionally graded material, Journal of Alloys and Compounds 838 (2020) 155322.
90. S.M. Thompson, L. Bian, N. Shamsaei, A. Yadollahi, An overview of direct laser deposition for additive manufacturing; part I: transport phenomena, modeling and diagnostics, Add. Manufact. 8 (2015) 36-62.
91. Y.L. Hu, X. Lin, X.B. Yu, J.J. Xu, M. Lei, W.D. Huang, Effect of Ti addition on cracking and microhardness of Inconel 625 during the laser solid forming processing, J. Alloys Compd. 711 (2017) 267e277, https://doi.org/10.1016/j.jallcom.2017.03.355.
92. C. Shang, C. Wang, G. Xu, C. Li, J. You Laser additive manufacturing of TA15 - Inconel 718 bimetallic structure via Nb/Cu multi-interlayer. Vacuum 169 (2019)108888.
93. M. Mukherjee, Effect of build geometry and orientation on microstructure and properties of additively manufactured 316L stainless steel by laser metal deposition, Materialia 7 (2019), 100359, https://doi.org/10.1016/j.mtla.2019.100359.

94. Y. Huang, M. Ansari, H. Asgari, M.H. Farshidianfar, D. Sarker, M.B. Khamesee, E. Toyserkani, Rapid prediction of real-time thermal characteristics, solidification parameters and microstructure in laser directed energy deposition (powder-fed additive manufacturing), J. Mater. Process. Technol. 274 (2019), 116286, https:// doi.org/10.1016/j.jmatprotec.2019.116286.

95. X. Zhang, T. Pan, A. Flood, Y. Chen, Y. Zhang, F. Liou, Investigation of copper/stainless steel multi-metallic materials fabricated by laser metal deposition, Materials Science & Engineering A 811 (2021) 141071.

96. G.P. Dinda, A.K. Dasgupta, J. Mazumder, Laser aided direct metal deposition of inconel 625 superalloy: microstructural evolution and thermal stability, Mat. Sci. Eng. A 509 (1-2) (2009) 98-104.

97. S. Scudino, C. Unterdörfer, K.G. Prashanth, H.Attar, N.Ellendt, V.Uhlenwinkel, J. Eckert Additive manufacturing of Cu–10Sn bronze Materials Letters 156 (2015) 202-204.

98. Amine, T., Newkirk, J.W., Liou, F., 2014b. An investigation of the effect of direct metal deposition parameters on the caracteristics of the deposited layers. Case Stud. Therm. Eng. 3, 21-34.

99. Liverani, E., Toschi, S., Ceschini, L., Fortunato, A., 2017. Effect of selective laser melting (SLM) process parameters on microstructure and mechanical properties of 316L austenitic stainless steel. J. Mater. Process. Technol. 249 (November), 255-263.

100. D.B. Williams, C.B. Carter, Transmission Electron Microscopy: A Textbook for Materials Science, second ed., Springer, New York, 2009.

101. L.D. Bobbio, B. Bocklund, A. Reichardt, R. Otis, J.P. Borgonia, R.P. Dillon, B. McEnerney, P. Hosemann, Z. Liu, A.M. Beese, Analysis of formation and growth of the s phase in additively manufactured functionally graded materials, J. Alloys Compd. 814 (2020) 151729, https://doi.org/10.1016/ j.jallcom.2019.151729.

102. INNOVATEST Falcon 500 Microhardness Tester, https://www.innovatest-europe.com/products/falcon-500/.

103. B.E. Carroll, T.A. Palmer, A.M. Beese, Anisotropic tensile behavior of Ti-6Al-4V components fabricated with directed energy deposition additive manufacturing, Acta Mat. 87 (2015) 309-320.

104. NETZSCH LFA 457 MicroFlash®, https://www.netzsch-thermal-analysis.com/en/products-solutions/thermal-diffusivity-conductivity/lfa-457-microflash/.
105. AURIBIS, Material Datasheet CuSn10, https://www.aurubis-stolberg.com/wdb/band/eng/Copper%20tin/CuSn10-PNA%20292_EN.pdf.
106. NETZSCH STA 449 F3 Jupiter®, https://www.netzsch-thermal-analysis.com/en/products-solutions/simultaneous-thermogravimetry-differential-scanning-calorimetry/sta-449-f3-jupiter/